

**Dielectric Permittivity Measurements of Thin Films at Microwave and Terahertz
Frequencies**

A thesis
submitted by

Liu Chao

In partial fulfillment of the requirements

for the degree of

Master of Science

in

Electrical Engineering

Tufts University

Date

August, 2012

ADVISOR:

Dr. Mohammed N. Afsar

Abstract

This thesis focuses on the complex dielectric characterizations of thin film materials using the state-of-the-art methods at microwave wavelengths and terahertz frequencies. Several methods are developed and employed.

Thin film materials are already used in a variety of microwave and higher frequency applications such as electrically tunable microwave devices, integrated circuits like MMICs, radomes, and radar absorbing coating. The determination of the dielectric properties of these films is thus of significant importance. The measurement of complex dielectric permittivity of thin films is very difficult at microwave, millimeter, and THz frequencies because both the amplitude change and phase shift are not large enough to evaluate the real part of the dielectric permittivity.

A specially designed transverse slotted cavity for X-band microwave measurement has been designed and constructed to employ with a vector network analyzer to evaluate the real part of dielectric permittivity of thin films accurately and conveniently. The dispersive Fourier transform spectroscopy (DFTS) with an improved 500 nanometer step mirror movement has been implemented to increase the phase change determination significantly to characterize the real part of permittivity from about 300 GHz to 700 GHz. Both techniques can record small phase shift caused by the thin film precisely. Commercially available polymer thin films are measured to validate the methods.

Table of Contents

Abstract.....	ii
List of Tables	v
List of Figures.....	vi
Acknowledgements.....	viii
1. Introduction.....	9
2. Dielectric Permittivity Measurement at Microwave Frequencies.....	11
2.1 Introduction	11
2.2 Waveguide Theory	12
2.3 Vector Network Analyzer.....	15
2.4 Determination of Scattering Parameters.....	17
2.5 In-waveguide Measurement	21
2.6 Open and Cavity Resonator.....	32
2.7 Slotted Cavity Measurement	36
2.8 Measurement Results	52
3. Dielectric Permittivity Measurement at Terahertz Frequency	57
3.1 Introduction	57
3.2 Dispersive Fourier Transform Spectroscopy.....	58
3.3 Improvement and Results.....	65
3.4 Discussion	70
3.5 Conclusion.....	76
4. Error Analysis	77

5. Conclusion	81
List of Publication.....	82
Reference	83

List of Tables

Table 1 Waveguide Modes and Conditions	14
Table 2 Measured Relative Permittivity of Several Thin Film Materials Using a Slotted Cavity .51	
Table 3 Relative Permittivity of Teflon (thickness = 0.001 inch).....	53
Table 4 Relative Permittivity of Black Polyester (thickness = 0.001 inch)	53
Table 5 Relative Permittivity of Mylar Polyester Film (thickness = 0.001 inch)	53
Table 6 Relative Permittivity of Polyphenylene Sulfide (thickness = 0.003 inch).....	54
Table 7 Relative Permittivity of Fluoropolymer Film (thickness = 0.001 inch).....	54
Table 8 Relative Permittivity of Polyethylene Film (thickness = 0.003 inch).....	55
Table 9 Relative Permittivity of Polyethylene Film (thickness = 0.005 inch).....	55
Table 10 Relative Permittivity of Acetal Polyoxymethylene Film (thickness = 0.003 inch)	55
Table 11 Relative Permittivity of Black Polyester (thickness = 0.001 inch)	56
Table 12 Relative Permittivity of Black Polyester (thickness = 0.00075 inch)	56
Table 13 Random Error in Transverse Slotted Cavity Method.....	77
Table 14 Comparison of Permittivity between DFST, Transverse Slotted Cavity and Other Literature.....	78

List of Figures

Figure 1: Signal flow inside the vector network analyzer showing how the data is measured and recorded.	16
Figure 2: Electromagnetic waves transmitting through and reflected from a sample in a transmission line	18
Figure 3: Setup of in-waveguide measurement method.....	22
Figure 4: Propagating TE ₁₀ mode wave inside the loaded material in-waveguide	29
Figure 5: Measured relative permittivity of black Kapton using in-waveguide measurement method.	32
Figure 6: The confocal Fabry-Perot open resonator for millimeter-wave dielectric measurement. S represents the specimen position. It is important that the specimen be positioned in the center and that the plane of the specimen be perpendicular to the axis of mirrors in the resonator. The shaded area shows the extent of the millimeter-wave beam in the resonator. [12]	33
Figure 7: The hemispherical type of open resonator for millimeter-wave dielectric measurement. The specimen in this case rests on the flat mirror of the resonator, thereby easing the specimen positioning requirement. It also allows a liquid specimen to be inserted over the flat mirror to form a plane parallel liquid layer. [12]	34
Figure 8: Pin hole cavity resonator for measurement of dielectric permittivity [13].	35
Figure 9: Longitudinal slotted waveguides for cavity resonators. The slots are in longitudinal direction.....	35
Figure 10: Transverse slotted X-band Waveguide. A transverse slot was made at the center transverse section of the waveguide.....	37
Figure 11: Slotted Cavity with Coupling Irises. Two irises are added to the slotted X-band waveguide in Figure 10.....	38
Figure 12: Setup for transverse slotted cavity measurement for the measurement at X-band. The cavity has a slot in the transverse direction.....	39
Figure 13: Dimension of the resonant cavity.....	40

Figure 14: Schematic curves of magnitude of electric field and magnetic field.....	48
Figure 15: Measured S_{21} of Slotted Cavity With and Without Teflon Sample showing the resonant frequencies.	51
Figure 16: Ray diagram of the dispersive Fourier transform interferometer. The beam division is accomplished by using a pair of free standing wire grid polarizers. One grid acts as a polarizer/analyzer and other grid as a beam divider and beam recombiner. Note that the specimen rests in one of the active mirror arm of the interferometer to provide the phase information in addition to the amplitude information.....	62
Figure 17: Set up for the measurement of thin film samples. The golden cylinder is the bolometer. The solid machine has been leveled to ensure optical alignment of all devices and sample holder.	65
Figure 18: Reference interferogram.without any thin film sample and shifted interferogram from Mylar thin film.	67
Figure 19: Relative real dielectric permittivity of Teflon thin film with 25.4 um thickness.	68
Figure 20: Relative real dielectric permittivity of Mylar thin film with 26.5 um thickness.	69
Figure 21: Relative real dielectric permittivity of black polyester thin film with 19 um thickness.	70
Figure 22: Multi-reflection diagram. O, S, M represent dry air, solid thin film, and mirror, respectively. R1 is the front specimen surface reflected beam, R2 is the back specimen surface reflected beam, T is the transmitted beam, and M are multiply reflected beams. Beams are in normal incidence, but shown at inclined incidence for figure clarity.	71
Figure 23: A schematic of the reference and specimen interferograms with multi-reflection. It shows not only one interferogram in the shifted interferogram pattern with sample.	72

Acknowledgements

I would like to thank my advisor Professor Mohammed N. Afsar for his all kinds of valuable help, advice, encouragement, time and support during my graduate studies. I am also very grateful to my committee members: Dr. Joshua L. Wilson and Dr. Douglas Preis.

I would like to thank MIT Lincoln Laboratory for the collaboration that has sponsored this work. Thanks to Dr. Joshua L. Wilson, Dr. Mohamed Abouzahra for their support. Thanks to my friends Benjamin Yu, Anjali Sharma and Dr. Konstantin Korolev for their help in this work.

1. Introduction

Although there are various well documented methods for determining the dielectric properties of low-loss ultra-thin films, finding methods that are applicable and sensitive enough for use on ultra-thin materials is a challenge. Close-ended coaxial probe technique is developed based on measuring the reflection coefficient from a coaxial transmission line. References [1, 2] take advantage of microstrip transmission lines and resonators. Dielectric resonator methods are also implemented on measuring properties of thin films [3-5].

The newly developed slotted cavity technique described in this paper can measure very thin materials around 1 mil (25.4 μm) thickness over microwave frequencies. A slotted cavity measurement scheme is shown here that employs a transverse slot in the narrow wall through which the sample can be inserted and removed. This method is much simpler and the sample occupies the entire cross section of the cavity. The transverse slot is more sensitive than longitudinal slot because the sample is oriented parallel to the wavefront, which can provide a reduced transmission and higher reflection.

Fourier spectroscopy has proven to be a viable method for broadband measurement of materials. In dispersive Fourier transform spectroscopy (DFTS), a spectrum is constructed by performing a numerical Fourier transform in the digitized interference pattern, recorded as a function of path difference within the interferometer.

This allowed the continuous spectrum for absorption and refraction to be mapped at any resolution over the entire millimeter, far-infrared, and mid-infrared region, hence linking the microwave world with mid- and near-infrared world.

Fourier spectrometers offered many advantages over the hugely popular grating spectrometers, in that they give both absorption and refraction data. Also, the optical and mechanical requirements of the Fourier spectrometer systems were less strict than those of the grating systems. Initially, the Fourier spectrometers were very successful in many areas that dealt with physics and chemistry; however, like the grating spectrometer, it could only provide absorption and refraction data at first. After some time, the need for a machine setup to provide a direct route to the absorption, refraction, and especially the permittivity data for frequencies above 30 GHz became evident.

The interferogram of a sample is measured and compared to a reference. It introduces a phase shift in addition to the amplitude loss. The dielectric properties of the sample shift and distort the interferogram signature. Using a double-sided complex Fourier transform, the phase and modulus spectra of the sample in question are produced. These data, along with a comparison to the reference interferogram, can be used to derive the refractive index and the real part of complex dielectric permittivity of the sample [5]. The technique was implemented for various materials such as solids, liquids, gases, magnetic materials, powders, composites, biological specimens, and materials at low and high temperatures. This technique can now be used routinely at our labs at Tufts

University at millimeter waves (even as long as 10 mm) as well as submillimeter and mid-infrared frequencies for the measurement of spectra for absorption coefficient, refractive index, real and imaginary parts of complex permittivity, and loss tangent with unprecedented precision. Dispersive Fourier transform spectroscopy can also be used for the measurement of real and imaginary parts of complex magnetic permeability of ferrites and magnetic materials[6].

An improvement on the active arm was made so the scanning mirror can now move in 500 nano meter steps. The resolution of the dispersive Fourier transform spectroscopy was improved to a higher stage. DFTS provides a broadband measurement of the permittivity of a sample at terahertz frequencies.

2. Dielectric Permittivity Measurement at Microwave Frequencies

2.1 Introduction

The measurement techniques described in this thesis on thin films in microwave frequency range are based on waveguide theory. The in-waveguide measurement, cavity measurement, transverse slotted cavity measurement are all employing the rectangular waveguides with Agilent 8510C vector network analyzer (VNA) to record the scattering parameters, frequency shift and quality factor. From the scattering parameters, frequency shift and quality factor, the complex permittivity of the thin films are determined.

2.2 Waveguide Theory

Waveguides are structures used to guide electromagnetic waves from point to point. Waveguides can be generally classified as either metal waveguides or dielectric waveguides. Metal waveguides normally take the form of an enclosed conducting metal pipe. The waves propagating inside the metal waveguide may be characterized by reflections from the conducting walls. The dielectric waveguide consists of dielectrics only and employs reflections from dielectric interfaces to propagate the electromagnetic wave along the waveguide. In the measurement methods described in this section, hollow metal waveguides are employed.

Given any time-harmonic source of electromagnetic radiation, the phasor electric and magnetic fields associated with the electromagnetic waves that propagate away from the source through a medium characterized by (ϵ, μ) must satisfy the source-free Maxwell's equations (in phasor form) given by

$$\nabla \times \vec{E} = -j\omega\mu\vec{H} \quad (1)$$

$$\nabla \times \vec{H} = j\omega\epsilon\vec{E} \quad (2)$$

The source-free Maxwell's equations can be manipulated into wave equations for the electric and magnetic fields (as was shown in the case of plane waves). These wave equations are

$$\nabla^2 \vec{E} + k^2 \vec{E} = 0, \quad (3)$$

$$\nabla^2 \vec{H} + k^2 \vec{E} = 0, \quad k = \omega \sqrt{\epsilon \mu} \quad (4)$$

where the wavenumber k is real-valued for lossless media and complex-valued for lossy media. The electric and magnetic fields of a general wave propagating in the $+z$ -direction (either unguided, as in the case of a plane wave or guided, as in the case of a transmission line or waveguide) through an arbitrary medium with a propagation constant γ , are characterized by a z -dependence of $e^{-\gamma z}$. The electric and magnetic fields of the wave may be written in rectangular coordinates as

$$\vec{E}(x, y, z) = \vec{E}_{xy}(x, y)e^{-\gamma z}, \quad (5)$$

$$\vec{H}(x, y, z) = \vec{H}_{xy}(x, y)e^{-\gamma z}, \quad \gamma = \alpha + j\beta \quad (6)$$

where α is the wave attenuation constant and β is the wave phase constant. The propagation constant is purely imaginary ($\alpha = 0, \gamma = j\beta$) when the wave travels without attenuation (no losses) or complex-valued when losses are present.

By expanding the curl operator of the source free Maxwell's equations in rectangular coordinates, we note that the derivatives of the transverse field components with respect to z are

$$\frac{\partial \vec{E}_x}{\partial z} = -\gamma \vec{E}_x, \quad \frac{\partial \vec{E}_y}{\partial z} = -\gamma \vec{E}_y, \quad \frac{\partial \vec{H}_x}{\partial z} = -\gamma \vec{H}_x, \quad \frac{\partial \vec{H}_y}{\partial z} = -\gamma \vec{H}_y. \quad (7)$$

If we equate the vector components on each side of the two Maxwell curl equations, we find

$$j\omega\varepsilon\vec{E}_x = \frac{\partial\vec{H}_z}{\partial y} + \gamma\vec{H}_y, -j\omega\varepsilon\vec{E}_y = \frac{\partial\vec{H}_z}{\partial x} + \gamma\vec{H}_x, j\omega\varepsilon\vec{E}_z = \frac{\partial\vec{H}_y}{\partial x} - \frac{\partial\vec{H}_x}{\partial y}, \quad (8)$$

$$-j\omega\varepsilon\vec{H}_x = \frac{\partial\vec{E}_z}{\partial y} + \gamma\vec{E}_y, -j\omega\varepsilon\vec{H}_y = \frac{\partial\vec{E}_z}{\partial x} + \gamma\vec{E}_x, j\omega\varepsilon\vec{H}_z = -\frac{\partial\vec{E}_y}{\partial x} + \frac{\partial\vec{E}_x}{\partial y}. \quad (8)$$

We may manipulate (8) and (9) to solve for the longitudinal field components in terms of the transverse field components.

$$\vec{E}_x = \frac{1}{h^2} \left(-\gamma \frac{\partial\vec{E}_z}{\partial x} - j\omega\mu \frac{\partial\vec{H}_z}{\partial y} \right), \vec{E}_y = \frac{1}{h^2} \left(-\gamma \frac{\partial\vec{E}_z}{\partial y} + j\omega\mu \frac{\partial\vec{H}_z}{\partial x} \right), \quad (10)$$

$$\vec{H}_x = \frac{1}{h^2} \left(j\omega\varepsilon \frac{\partial\vec{E}_z}{\partial y} - \gamma \frac{\partial\vec{H}_z}{\partial x} \right), \vec{H}_y = \frac{1}{h^2} \left(-j\omega\varepsilon \frac{\partial\vec{E}_z}{\partial x} - \gamma \frac{\partial\vec{H}_z}{\partial y} \right). \quad (11)$$

where the constant h is defined by $h^2 = \gamma^2 + \omega^2\mu\varepsilon = \gamma^2 + k^2 \Rightarrow \gamma = \sqrt{h^2 - k^2}$.

The equations for the transverse fields in terms of the longitudinal fields describe the different types of possible modes for guided and unguided waves.

Table 1 Waveguide Modes and Conditions

Transverse electromagnetic (TEM)	$\vec{E}_z = 0, \vec{H}_z = 0$	Hollow waveguide does not support TEM mode
Transverse electric (TE)	$\vec{E}_z = 0, \vec{H}_z \neq 0$	TE mode
Transverse magnetic (TM)	$\vec{E}_z \neq 0, \vec{H}_z = 0$	TM mode

Hybrid	$\vec{E}_z \neq 0, \vec{H}_z \neq 0$	EH or HE mode
--------	--------------------------------------	---------------

For simplicity, consider the case of guided or unguided waves propagating through an ideal (lossless) medium where k is real-valued. For TEM modes, the only way for the transverse fields to be non-zero with $\vec{E}_z = 0, \vec{H}_z = 0$ is for $h = 0$. For the waveguide modes (TE, TM or hybrid modes), h cannot be zero since this would yield unbounded results for the transverse fields. Thus, the waveguide propagation constant can be written as

$$\gamma = \sqrt{h^2 - k^2} = \sqrt{-k^2 \left(1 - \frac{h^2}{k^2}\right)} = jk \sqrt{1 - \left(\frac{h}{k}\right)^2}. \quad (12)$$

The propagation constant of a wave in a waveguide (TE or TM waves) has very different characteristics than the propagation constant for a wave in TEM modes. The ratio of h/k in the waveguide mode propagation constant equation can be written in terms of the cutoff frequency f_c for the given waveguide mode as follows,

$$\frac{h}{k} = \frac{h}{\omega \sqrt{\mu \epsilon}} = \frac{h}{2\pi f \sqrt{\mu \epsilon}} = \frac{f_c}{f}, f_c = \frac{h}{2\pi \sqrt{\epsilon \mu}}.$$

2.3 Vector Network Analyzer

A two ports Vector Network Analyzer is used to characterize two port networks. In this study, it was employed to characterize the thin film material under test, which was loaded in waveguides or transverse slotted cavity to form the two port network. An

accurate measurement involves standardization and calibration of the system at the required frequencies and ambient conditions. Here, measurement was carried out from 2 to 40 GHz. The network analyzer includes a signal source, a receiver and a display unit to process the signals. The block diagram of network analyzer is shown in Figure 1.

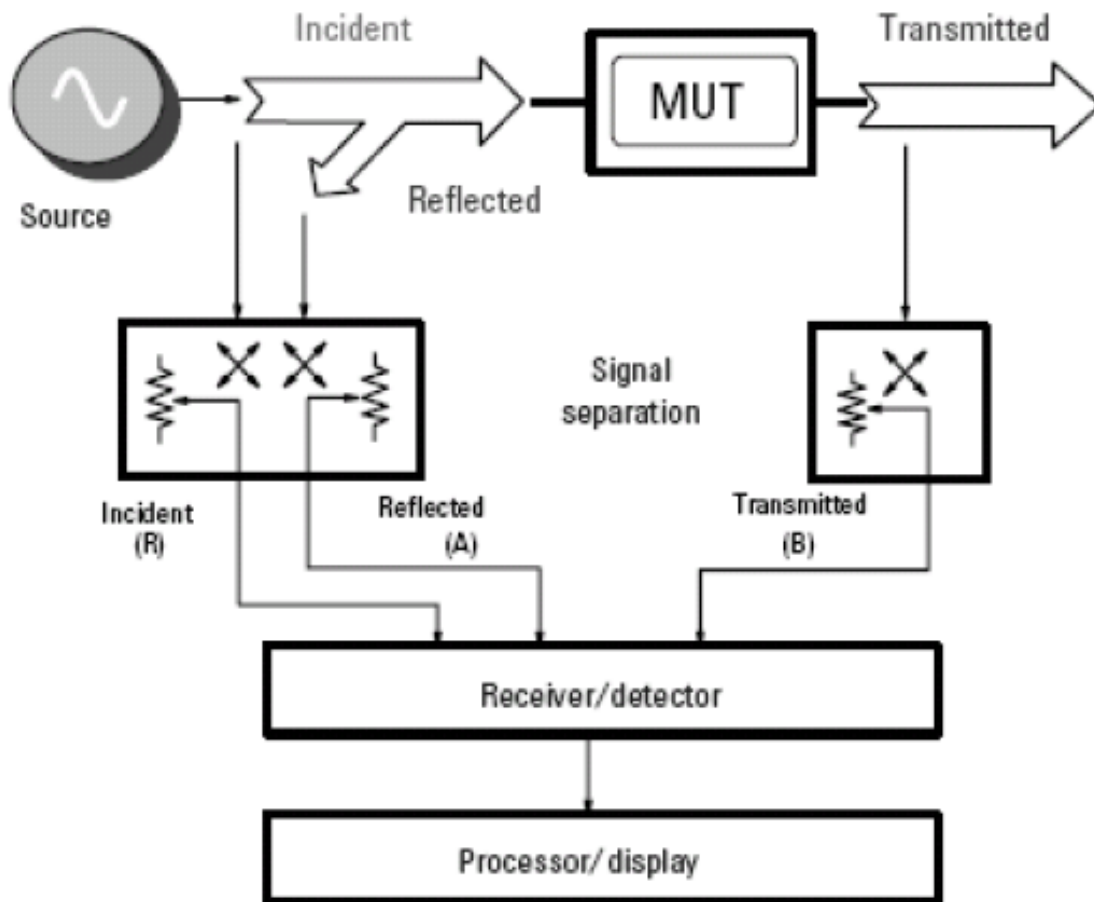


Figure 1: Signal flow inside the vector network analyzer showing how the data is measured and recorded.

The source launches a RF signal at a single frequency towards the sample under test. The test set separates the signal produced by the source into an incident signal, sent

to the sample under test, and a reference signal against which the transmitted and reflected signals are later compared. The test set routes the transmitted and reflected signals from the material under test to the receiver. The receiver is tuned to the frequency of the RF signal provided by the source. The source is then stepped to the next frequency and the measurement is repeated to display the reflection and transmission response as a function of frequency. The measured response produces the magnitude and phase for each scattering parameter at that frequency.

The following techniques can be used with the network analyzer for electromagnetic measurements: Free space measurement, Resonant Cavity Measurement, In-Waveguide Measurement, Open-ended waveguide measurement. In this dissertation, in-waveguide measurement method and transverse slotted cavity measurement are showed.

2.4 Determination of Scattering Parameters

When a transmission line is terminated in a load, standing waves are generated inside the line. The amplitude and location of the maxima and minima in the slotted section depend on the load. The impedance is computed from the shift in null of the standing wave pattern inside the slotted section which is then used to compute the permittivity and permeability of the material. But characterization of the material becomes complicated when it shows dielectric and magnetic properties simultaneously.

To characterize such materials like ferrites, one requires the measurement of four independent quantities and the complex reflection coefficient is then calculated from the scattering parameters.

Consider the measurement configuration shown in Figure 2. The sample of length L is placed inside a transmission line. Port 1 and 2 represent the measurement ports for the VNA, whereas the actual measurements are desired at interfaces 1 and 2. To analyze the propagation of the incident wave, the whole setup is divided into three sections as shown in Figure 2. Thus region I consists of the wave incident at and reflected from material interface 1, region II corresponds to the wave travelling inside the material and region III consists of the transmitted wave. For simplicity, only one reflection has been shown.

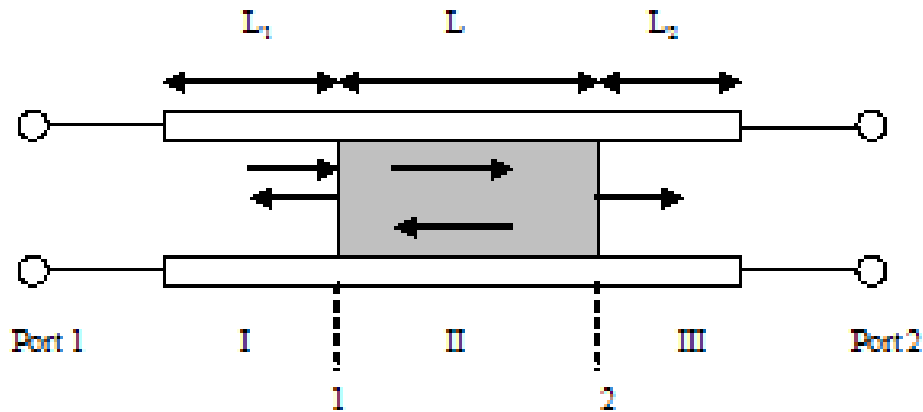


Figure 2: Electromagnetic waves transmitting through and reflected from a sample in a transmission line

Using electromagnetic theory, for a wave incident in region I we can write the expressions for the field in each section as [7]:

$$\begin{aligned}
 E_I &= C_1 \exp(-\gamma_0 x) + C_2 \exp(\gamma_0 x) \\
 E_{II} &= C_3 \exp(-\gamma x) + C_4 \exp(\gamma x) \\
 E_{III} &= C_5 \exp(-\gamma_0 x)
 \end{aligned} \tag{13}$$

γ and γ_0 are the propagation constants in the transmission line with and without the sample, respectively. These are evaluated as,

$$\begin{aligned}
 \gamma &= j \sqrt{\frac{\omega_2 \mu_r \epsilon_r}{c^2} - \left(\frac{2\pi}{\lambda_c}\right)^2} \\
 \gamma_0 &= j \sqrt{\left(\frac{\omega}{c}\right)^2 - \left(\frac{2\pi}{\lambda_c}\right)^2}
 \end{aligned} \tag{14}$$

where ω is the angular frequency, c is the speed of light in vacuum and λ_0 is the cutoff wavelength of the transmission line. The constants C_i mentioned in the Equation (13) can be determined from the boundary conditions at the interface. The boundary condition on the electric field is the continuity of the tangential component at the interfaces:

$$\begin{aligned}
 E_I \Big|_{x=L_1} &= E_{II} \Big|_{x=L_1} \\
 E_{II} \Big|_{x=L_1+L} &= E_{III} \Big|_{x=L_1+L}
 \end{aligned} \tag{15}$$

where, L_1 and L_2 are the distances of the respective ports from the sample faces. The boundary condition on the magnetic field requires an additional assumption that no surface currents are generated so that the tangential component of magnetic field is continuous across the interface:

$$\frac{1}{\mu_0} \frac{\partial E_I}{\partial x} \Big|_{x=L_1} = \frac{1}{\mu_0 \mu_r} \frac{\partial E_{II}}{\partial x} \Big|_{x=L_1} \quad (16)$$

$$\frac{1}{\mu_0 \mu_r} \frac{\partial E_{II}}{\partial x} \Big|_{x=L_1+L} = \frac{1}{\mu_0} \frac{\partial E_{III}}{\partial x} \Big|_{x=L_1+L}$$

These boundary conditions are applied to the electric field equations to find a solution for the s-parameters of the two-port network. Since the scattering matrix is symmetric, $S_{12} = S_{21}$ and we have,

$$\begin{aligned} S_{11} &= R_1^2 \frac{\tau(1-T^2)}{1-\tau^2 T^2} \\ S_{12} = S_{21} &= R_1 R_2 \frac{\tau(1-T^2)}{1-\tau^2 T^2} \\ S_{22} &= R_2^2 \frac{\tau(1-T^2)}{1-\tau^2 T^2} \end{aligned} \quad (17)$$

where R_1 and R_2 are the reference plane transformations at the two ports, given by:

$$R_i = \exp(-\gamma_0 L_i) \quad (18)$$

The transmission (T) and reflection (R) coefficients are calculated using,

$$T = \exp(-\gamma L) \quad (19)$$

$$\tau = \frac{\begin{pmatrix} \gamma_0 \\ \mu_0 \end{pmatrix} - \begin{pmatrix} \gamma \\ \mu \end{pmatrix}}{\begin{pmatrix} \gamma_0 \\ \mu_0 \end{pmatrix} + \begin{pmatrix} \gamma \\ \mu \end{pmatrix}} \quad (20)$$

Additionally, S_{21} for the empty sample holder is $S_{21}^0 = R_1 R_2 \exp(-\gamma_0 L)$.

So this approach gives us nine real equations for five unknowns in case of non-magnetic materials and seven unknowns in case of magnetic materials. Thus the system of equations is over determined and the equations can be solved in different ways. [8]

2.5 In-waveguide Measurement

Here, a transmission reflection (T/R) based waveguide technique was used to carry out the measurements. The T/R method is a category of non-resonant methods that are widely used for the measurements of electromagnetic properties of materials. In this method, the sample under test is inserted into a segment of transmission line, such as waveguide or coaxial line, which forms the two port network shown in Figure 3. The cables from the network analyzer are connected to across this network. The Vector Network Analyzer records the s-parameter values. Scattering equations are used to analyze the fields at the sample interfaces. These equations relate the s-parameters of the segment of transmission line filled with the sample under study to the permittivity and permeability of that sample. In T/R method, all the four s-parameters can be measured, so we have a record of more data than what we have in reflection measurements.

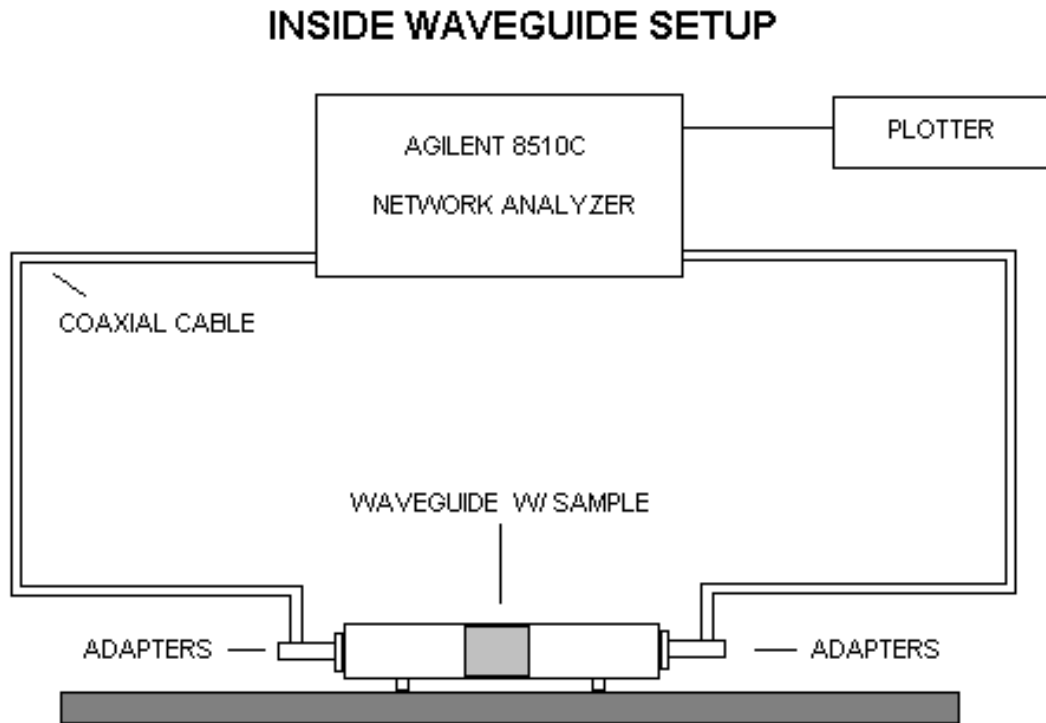


Figure 3: Setup of in-waveguide measurement method.

Several algorithms have been developed for determining the permittivity and permeability of the sample by Nicolson, Ross [9], Weir [10] and James Baker-Jarvis [7]. These algorithms were further improved in the Millimeter and Sub-Millimeter Waves Laboratory at Tufts University to increase the accuracy of the measurements [11].

Nicolson and Ross combined the equations for S_{11} and S_{21} and derived explicit formulas for the calculation of permittivity and permeability. First, the reflection coefficient for the incident wave was calculated as:

$$\tau = X \pm \sqrt{X^2 - 1} \quad (21)$$

where, $X = \frac{1 - V_1 V_2}{V_1 - V_2}$

$$\begin{aligned} V_1 &= S_{21} + S_{11} \\ V_2 &= S_{21} - S_{11} \end{aligned} \quad (22)$$

The complex magnetic permeability and dielectric permittivity were then determined as:

$$\begin{aligned} \mu_r &= \left(\frac{1 + \tau}{1 - \tau} \right) \frac{c}{\omega L} \ln \frac{1}{T} \\ \varepsilon_r &= \left(\frac{1 - \tau}{1 + \tau} \right) \frac{c}{\omega L} \ln \left(\frac{1}{T} \right) \end{aligned} \quad (23)$$

where, L is the length of the sample and transmission coefficient, $T = \frac{V_1 - \tau}{1 - V_1 \tau}$.

Nicolson and Ross derived S_{21} and S_{11} for time domain measurements using Fourier transform. This method had two major shortcomings. First, the determination of permeability and permittivity is band-limited, depending on the time response of the pulse and its repetition frequency. Secondly, in using discrete Fourier transform, errors arise due to truncation and aliasing.

Wier, in 1974, presented an analogous method for determination of complex permeability and permittivity in frequency domain for a wide range from 100 MHz to 18 GHz. He formulated the formulas for complex permeability and permittivity as,

$$\mu_r = \frac{1 + \tau}{(1 - \tau) \Lambda \sqrt{\left(\frac{1}{\lambda_0^2}\right) - \left(\frac{1}{\lambda_c^2}\right)}} \quad (24)$$

$$\varepsilon_r = \frac{\lambda_0^2}{\mu_r \left[\left(\frac{1}{\lambda_c^2}\right) - \left(\frac{1}{\Lambda^2}\right) \right]}$$

with $\frac{1}{\Lambda^2} = -\left[\frac{1}{2\pi L} \ln\left(\frac{1}{T}\right) \right]^2$, λ_0 is the free space wavelength and λ_c is the cut-off wavelength if the transmission line section.

It should be noted here that Equation (24) has an infinite number of roots. This equation is ambiguous since the phase of the transmission coefficient remains unaffected if the sample length changes by a multiple of wavelength.

To overcome this ambiguity, Weir introduced the use of group delay to accurately determine permeability and permittivity. Group delay through the material is strictly a function of the total length of the material. Therefore phase ambiguity can be resolved by finding a solution for permeability and permittivity from which a value of group delay is computed using,

$$\tau_{g,n} = L \frac{d}{df} \left(\frac{\varepsilon_r \mu_r}{\lambda_0^2} - \frac{1}{\lambda_c^2} \right)_n^{\frac{1}{2}} \quad (26)$$

The value of group delay thus computed is compared with the measured value of group delay, which is determined from the slope of the phase of the transmission coefficient (ϕ) versus frequency using the following equation,

$$\tau_g = -\frac{1}{2\pi} \frac{d\phi}{df} \quad (27)$$

The correct root should satisfy $\tau_{g,n} - \tau_g = 0$.

Thus phase ambiguity at each frequency is resolved by matching the calculated and measured group delay. But this is not a very consistent method. In the measurements performed in this study, a phase unwrapping technique was used to resolve this phase ambiguity. Whenever the jump in the value of phase from one measurement frequency to the next is more than π , all the subsequent phases are shifted by 2π in the opposite direction.

A drawback in the Nicolson-Ross-Weir algorithm was that in low loss materials at frequencies corresponding to integer multiples of half wavelengths, the solutions provided were observed to be divergent. At these frequencies, the scattering parameter $|S_{11}|$ becomes very small, making the equations algebraically unstable as $S_{11} \rightarrow 0$. Since the solution is proportional to $\left(\frac{1}{S_{11}}\right)$, the phase error dominates the solution at these frequencies. Many researchers use samples that have a length less than $n\lambda/2$ at the highest measurement frequency to resolve this issue. But the use of thin samples lowers the

measurement sensitivity due to uncertainty in reference plane positions. James Baker-Jarvis proposed an iterative procedure for obtaining stable measurements. This procedure minimizes the instability of the equations used by Nicolson-Ross-Weir and allows measurements to be taken on samples of arbitrary length. Baker-Jarvis used an iterative method on a set of equations to give a solution that is stable over the measurement spectrum. Sample length and air length are treated as unknowns in this system of equations. The solution is therefore independent of reference plane position, air line length and sample length. It was found that for cases where the sample length and reference plane positions are known to high accuracy, taking various linear combinations of the scattering equations and solving the equations in an iterative fashion yields a very stable solution on samples of arbitrary length. For example, one useful combination is,

$$\frac{1}{2} \{ [S_{12} + S_{21}] + \beta [S_{11} + S_{22}] \} = \frac{z(1 - \tau^2) + \beta\tau(1 - z^2)}{1 - z^2\tau^2} \quad (28)$$

where, β varies as a function of sample length, uncertainty in s-parameter values and loss characteristics of material. For low loss materials, S_{21} is strong and β is zero whereas for high loss materials S_{11} dominates, so large value of β is appropriate. In general, β is given by ratio of the uncertainty in S_{21} to S_{11} uncertainty.

All the modifications suggested so far either needed initial guess parameters or choice of appropriate integer values of phase. A novel technique for the measurement of thin samples using a modified propagation constant was developed at the Tufts Millimeter and Sub-Millimeter Waves laboratory. This method does not require initial

guess parameters, thus making the measurement set up more accurate. The modified s-parameters used in the measurements in this work are given below,

$$\begin{aligned}\tilde{S}_{11} &= S_{11} e^{j(0 \times \sqrt{k_0^2 - k_c^2})} \\ \tilde{S}_{21} &= S_{21} e^{j((l-d) \times \sqrt{k_0^2 - k_c^2})}\end{aligned}\quad (29)$$

where, l is the quarter wavelength difference between thru and line (in air), d is the thickness of the sample inside the waveguide, k_0 is the wavenumber of the sample and k_c is the cutoff wavenumber. These equations take into account the effect of using samples with thickness (d) values that are smaller than the waveguide shim used in the experimental setup. [8]

Return losses of less than -50 dB from the air inside the waveguide are easily achieved using these calibration techniques. This enables us to neglect any unwanted reflections from the inner walls of the waveguide when analyzing the S-parameters. The reflection and transmission by the scattering parameters inside the waveguide, in which the transmission and reflection resemble the free space formulation, can now be presented as follows:

$$\begin{aligned}\Gamma &= K \pm \sqrt{K^2 - 1} \\ K &= \frac{\tilde{S}_{11}^2 - \tilde{S}_{21}^2 + 1}{2\tilde{S}_{11}} \\ T &= \frac{\tilde{S}_{11} + \tilde{S}_{21} - \Gamma}{1 - (\tilde{S}_{11} + \tilde{S}_{21})\Gamma}.\end{aligned}\quad (30)$$

The transmission coefficient through the material may also be written as $T = e^{-\gamma d} = e^{-(\alpha + j\beta)d}$. The propagation constant through the material inside the waveguides has been derived to be:

$$\gamma_{TE_{10}} = \frac{\ln\left(\frac{1}{|T|}\right)}{d} + j\left(\frac{2\pi n - \phi_T}{d}\right) \quad (31)$$

Normally, a sample thickness of less than one quarter wavelength is desirable in this setup, because it will make $n = 0$. In order to achieve our goal and derive the complex permeability and permittivity for the loaded material inside the waveguide, we must determine the propagation constant through the material inside the waveguide. To achieve this, one must solve Maxwell's equations with respect to E_y for the TE_{10} mode as shown in Figure 4.

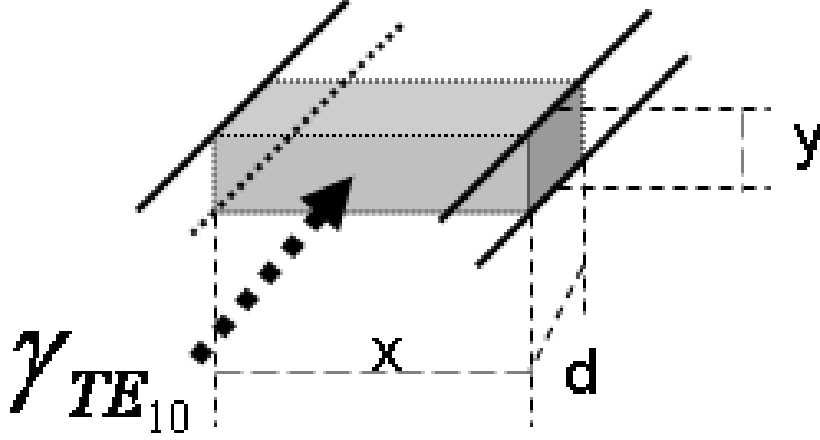


Figure 4: Propagating TE₁₀ mode wave inside the loaded material in-waveguide

$$\left(\frac{\partial}{\partial x'^2} + \frac{\partial}{\partial y'^2} + \beta^2\right)E_y = 0 \quad (32)$$

where $x' = x \frac{1}{\sqrt{\mu\epsilon}}$ and $y' = y \frac{1}{\sqrt{\mu\epsilon}}$

Solving Maxwell's equation yields:

$$E_y = C \sin(\beta_x x') \cos(\beta_y y') \quad (33)$$

where C is a constant to be determined from the boundary conditions. The boundary condition tells us that the propagation constant components may be presented as follows:

$$\gamma_0 = \frac{2\pi}{\lambda_0}, \quad \beta_x = \frac{n\pi}{a} \sqrt{\mu\epsilon} \quad \text{and} \quad \beta_y = \frac{m\pi}{b} \sqrt{\mu\epsilon} \quad (34)$$

This yields the following relationship for the propagation constant through the material inside the waveguide:

$$\gamma^2 = \gamma_0^2 - \beta_x^2 - \beta_y^2 \quad (35)$$

The propagation constant of the TE₁₀ is thus:

$$\begin{aligned} \gamma_{TE_{10}} &= j2\pi \sqrt{\left(\frac{1}{\lambda_0}\right)^2 - \left(\frac{1}{2a}\right)^2} \cdot \sqrt{\mu\varepsilon} = j\gamma_{TE_{10}}^0 \frac{\mu}{\eta} \\ \gamma_{TE_{10}}^0 &= \sqrt{\left(\frac{1}{\lambda_0}\right)^2 - \left(\frac{1}{2a}\right)^2} \end{aligned} \quad (36)$$

The complex permeability and permittivity associated with the propagation constant are then:

$$\mu = \frac{\eta\gamma_{TE_{10}}}{j\gamma_{TE_{10}}^0} = -j \left(\frac{1+\Gamma}{1-\Gamma} \right) \left(\frac{1}{2\pi d} \right) \left(\frac{\ln\left(\frac{1}{|T|}\right) + j(2\pi m - \varphi_T)}{\sqrt{\left(\frac{1}{\lambda_0}\right)^2 - \left(\frac{1}{2a}\right)^2}} \right) \quad (37)$$

$$\varepsilon = \frac{\mu}{Z_{TE}^2} = \frac{\mu}{\eta^2} \left(\lambda_0^2 \left(\frac{1}{\lambda_0^2} - \frac{1}{4a^2} \right) \right) \quad (38)$$

In our waveguide measurement technique the propagating wave was assumed to be the TE₁₀ mode. Permittivity is then calculated as follows:

$$\varepsilon = -j \left(\frac{c}{f} \right)^2 \left(\frac{1-\Gamma}{1+\Gamma} \right) \left(\frac{1}{2\pi d} \right) \left(\ln\left(\frac{1}{|T|}\right) + j(2\pi m - \varphi_T) \right) \left(\sqrt{\left(\frac{1}{\lambda_0}\right)^2 - \left(\frac{1}{2a}\right)^2} \right) \quad (39)$$

It was also noticed that the permeability and permittivity of the loaded sample affect the cut-off frequency for the waveguide band. This was accounted for in the calculations by including the cut-off frequency for each band in the derivation of permeability and permittivity from the data for s-parameters. The divergence in data was eliminated by using the electrical delay function of the network analyzer. The experiments carried out in the lab suggest that these modifications are necessary and known materials were measured to confirm the accuracy of the measurement technique. The derived permeability and permittivity data is very reliable and not affected by the scattering voltage ratios of the vector network analyzer.

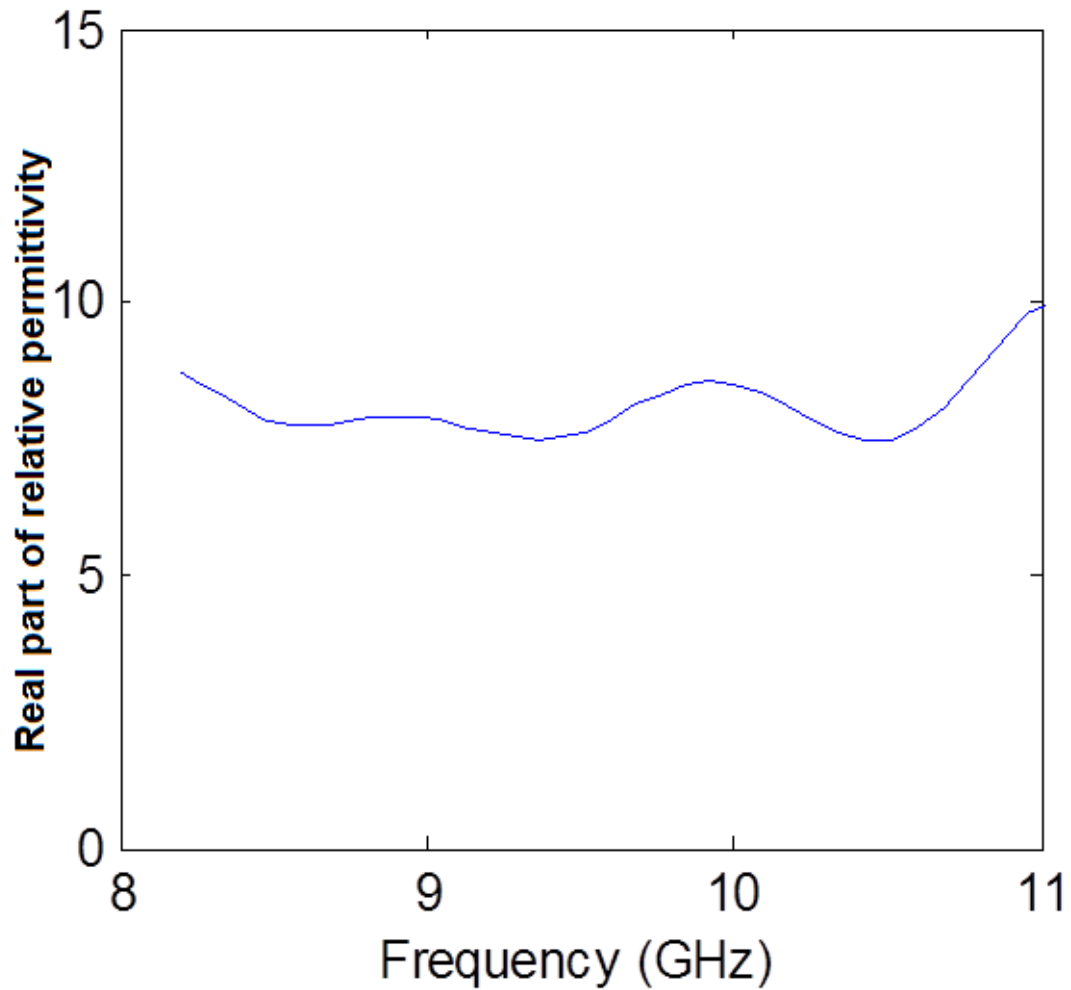


Figure 5: Measured relative permittivity of black Kapton using in-waveguide measurement method.

2.6 Open and Cavity Resonator

Resonators are employed in characterization of dielectric permittivity of materials. A resonator is a device or system that exhibits resonance or resonant behavior, that is, it naturally oscillates at some frequencies, called its resonant frequencies, with

greater amplitude than at others. Usually, open resonator and cavity resonator are used in material characterization.

Open resonator is an oscillatory system formed by a set of mirrors in which weakly damped electromagnetic oscillations in the optical and high frequency ranges can be excited and maintained, with radiation into free space. Fabry-Perot cavity is a typical open resonator. Various types of Fabry-Perot open resonator configurations can be adapted from two reflectors. Figure 6 shows a confocal Fabry-Perot open resonator. Figure 7 shows a hemispherical type of open resonator. A quality factor (Q) value greater than 100000 can be easily attained with a very small coupling hole.

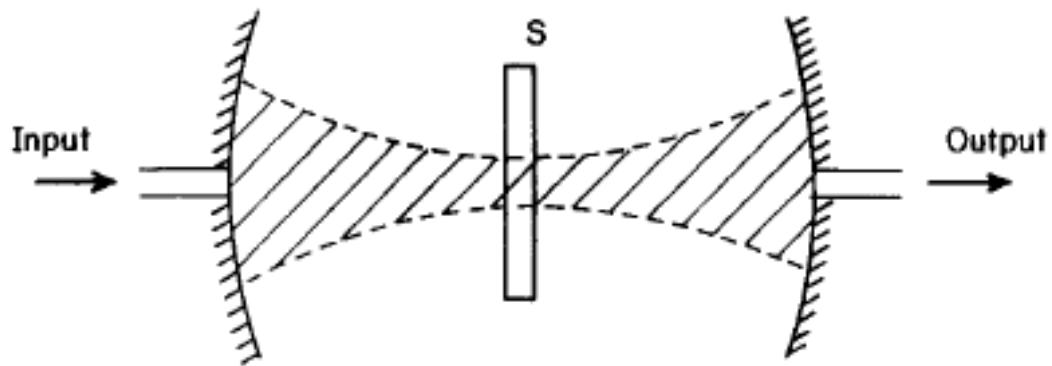


Figure 6: The confocal Fabry-Perot open resonator for millimeter-wave dielectric measurement. S represents the specimen position. It is important that the specimen be positioned in the center and that the plane of the specimen be perpendicular to the axis of mirrors in the resonator. The shaded area shows the extent of the millimeter-wave beam in the resonator. [12]

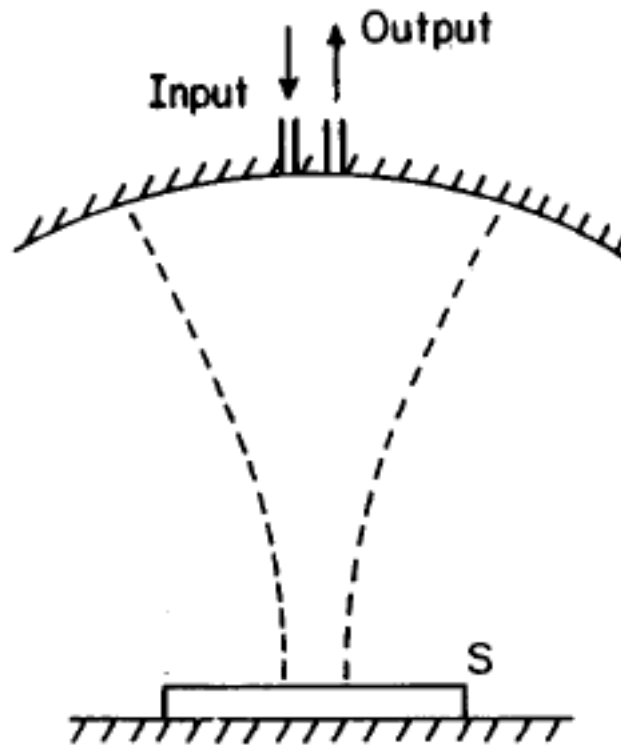


Figure 7: The hemispherical type of open resonator for millimeter-wave dielectric measurement. The specimen in this case rests on the flat mirror of the resonator, thereby easing the specimen positioning requirement. It also allows a liquid specimen to be inserted over the flat mirror to form a plane parallel liquid layer. [12]

A cavity resonator is a hollow conductor blocked at both ends and along which an electromagnetic wave can be supported. It can be viewed as a waveguide short-circuited at both ends. Figure 8 shows a pin hole waveguide cavity resonator and Figure 9 shows longitudinal slotted waveguide for cavity resonator.

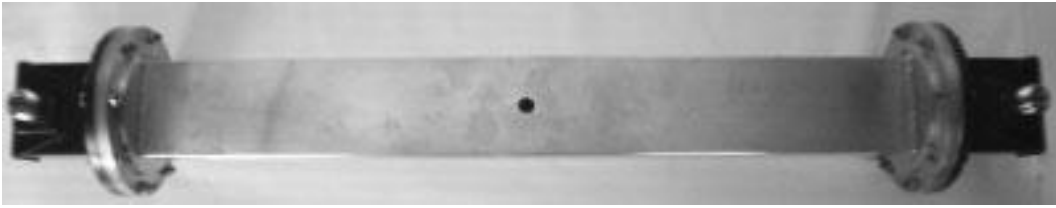


Figure 8: Pin hole cavity resonator for measurement of dielectric permittivity [13].



Figure 9: Longitudinal slotted waveguides for cavity resonators. The slots are in longitudinal direction.

These resonator measurement instruments can provide very high Q factor. However, their designs are not convenient for thin film materials. Therefore, a cavity resonator for thin film measurement is designed and fabricated.

2.7 Slotted Cavity Measurement

In this section, a special designed transverse slotted cavity is built in X-band. It was applied to determine the complex permittivity of thin film materials by employing perturbation theory.

The slotted cavity technique is a combination of in-waveguide method and cavity method. The cavity method employs waveguide with a hole where the cylinder sample can be inserted in the waveguide. Each cavity has resonant frequencies depending on the dimension of the cavity. The inserted sample will slightly change the distribution of electromagnetic fields inside the cavity thus change the resonant frequency and quality factor.

However, a key difference in this transverse slotted cavity method compared to the traditional cavity method is that slots can be made in the waveguide wall transverse to wave propagation direction through which the sample can be fed into the waveguide [2]. This allows a very accurate measurement of the difference in scattering parameters with and without the sample in place which, in turn, allows for much greater measurement

sensitivity. It is similar to a perturbation technique in that differences in scattering parameters are used in the calculations rather than the scattering parameters themselves.

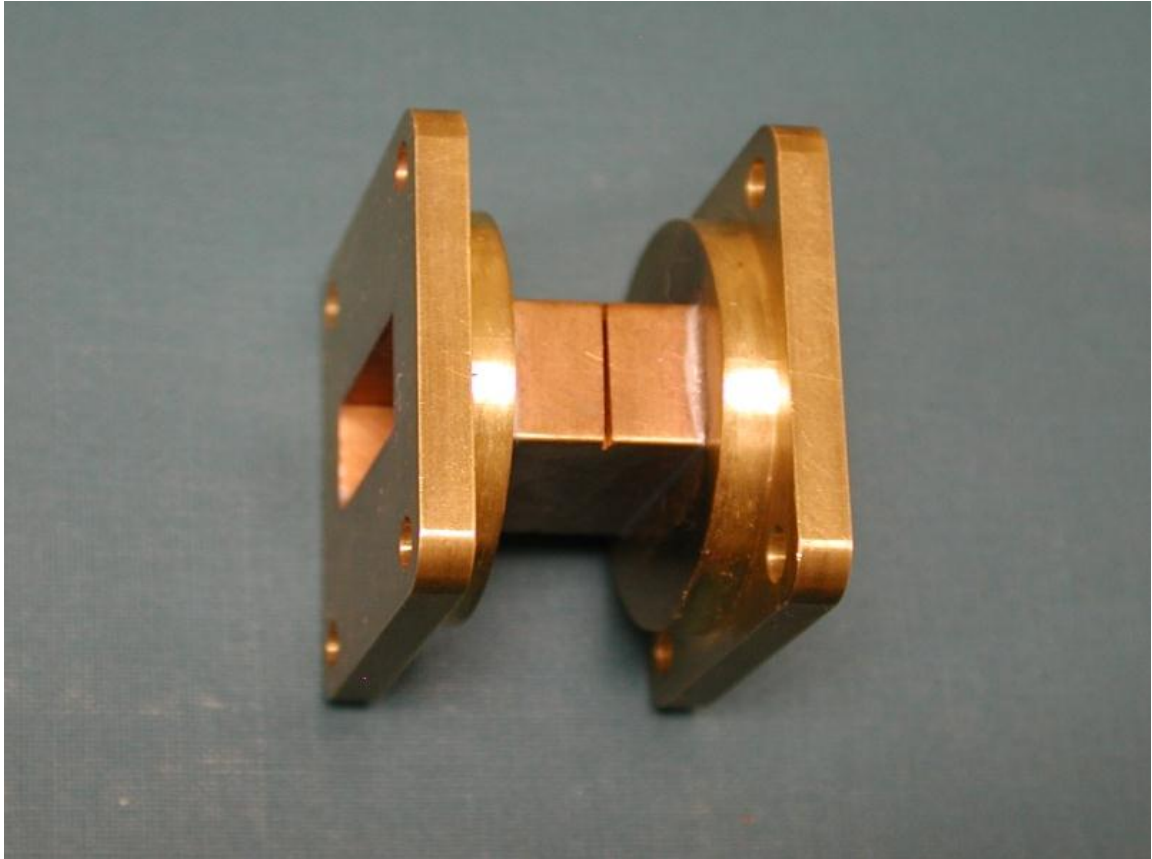


Figure 10: Transverse slotted X-band Waveguide. A transverse slot was made at the center transverse section of the waveguide.

Figure 10 shows the WR-90 slotted X-band waveguide used for the measurement. The waveguide is 1" long with the sample placed at the center. The sample is fed through narrow slots in both side walls (rather than the longitudinal slot of [2]) prior to the first measurement. It is held taut by pulling on both ends of the sample. This novel approach enabled the sample to stay in place without foam or Teflon supports. After the first

measurement is taken, the sample is removed through one of the slots, and a second measurement is taken of the system without the sample.

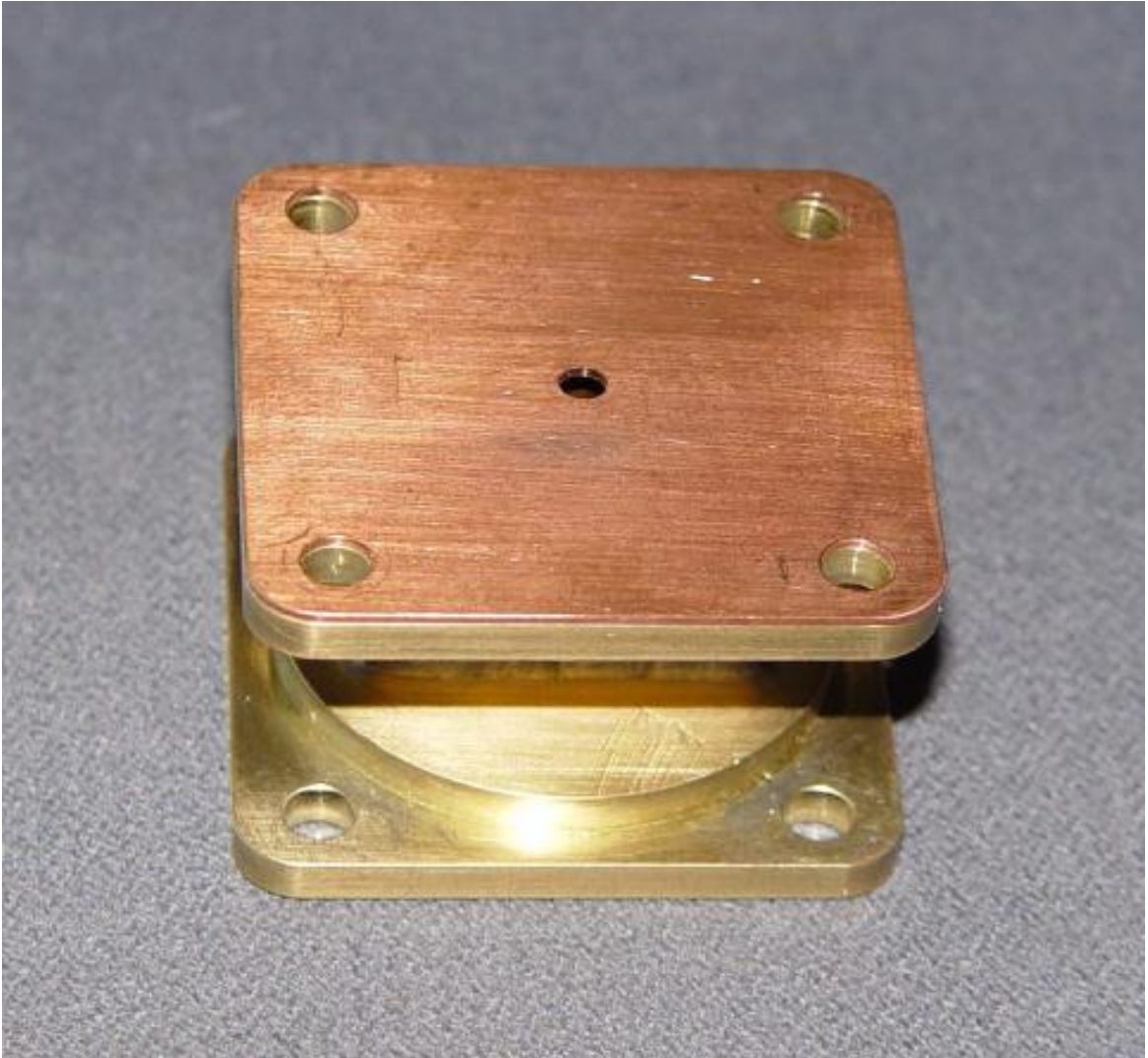


Figure 11: Slotted Cavity with Coupling Irises. Two irises are added to the slotted X-band waveguide in Figure 10.

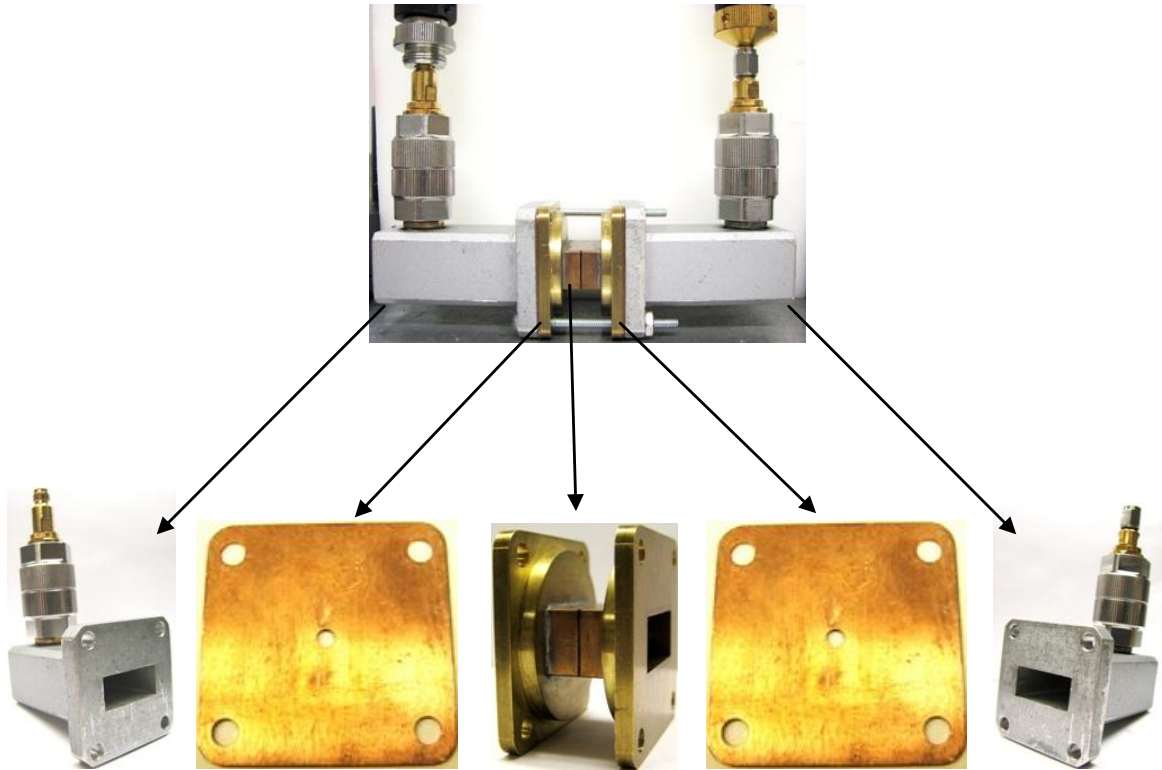


Figure 12: Setup for transverse slotted cavity measurement for the measurement at X-band. The cavity has a slot in the transverse direction.

The transverse slotted cavity comes from the rectangular waveguide resonator. This resonator is basically a section of rectangular waveguide which is enclosed on both ends by conducting irises to form an enclosed conducting box. We assume the same cross-sectional dimensions as the rectangular waveguide (a , b) and define the longitudinal length of the resonator as c shown in Figure 13. Given the conducting walls on the ends of the waveguide, the resonator modes may be described by waveguide modes which are reflected back and forth within the resonator ($+z$ and $-z$ directions) to form standing waves.

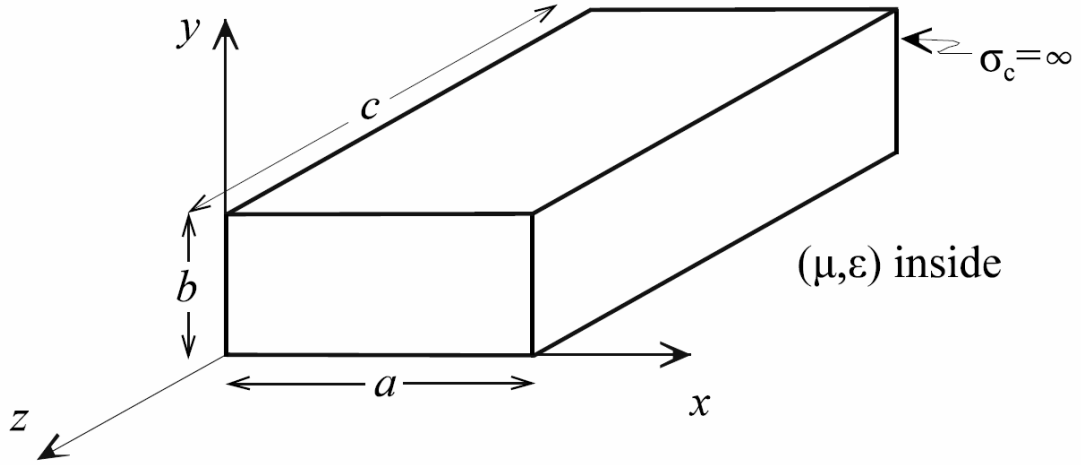


Figure 13: Dimension of the resonant cavity.

The standing waves in the cavity can be derived from section 2.2 as

$$\vec{H}_z(x, y, z) = H_0 \cos \frac{m\pi x}{a} \cos \frac{n\pi y}{b} (A \sin k_z z + B \cos k_z z) \quad (\text{TE modes}), \quad (40)$$

$$\vec{E}_z(x, y, z) = E_0 \sin \frac{m\pi x}{a} \sin \frac{n\pi y}{b} (C \sin k_z z + D \cos k_z z) \quad (\text{TM modes}). \quad (41)$$

The separation equation for the cavity modes is

$$k^2 = k_x^2 + k_y^2 + k_z^2 \quad (\text{separation equation}). \quad (42)$$

The cavity boundary conditions (in addition to the boundary conditions satisfied by the rectangular waveguide wave functions) are

$$\vec{E}_x(x, y, 0) = \vec{E}_y(x, y, 0) = 0, \quad (43)$$

$$\vec{E}_x(x, y, c) = \vec{E}_y(x, y, c) = 0. \quad (44)$$

From the source-free Maxwell's curl equations, the TE and TM boundary

conditions on the end walls of the cavity are satisfied if

$$\vec{H}_z(x, y, 0) = \vec{H}_z(x, y, c) = 0 \quad (\text{TE modes}), \quad (45)$$

$$\left. \frac{\partial \vec{E}_z(x, y, z)}{\partial z} \right|_{z=0} = \left. \frac{\partial \vec{E}_z(x, y, z)}{\partial z} \right|_{z=c} = 0 \quad (\text{TM modes}). \quad (46)$$

Application of the TE and TM boundary conditions yields

$$\vec{H}_z(x, y, 0) = 0 \Rightarrow B = 0, \quad (47)$$

$$\vec{H}_z(x, y, c) = 0 \Rightarrow k_z c = p_{1,2,3,\dots} \pi \Rightarrow k_z = \frac{p\pi}{c}, \quad (48)$$

$$\vec{E}_z(x, y, 0) = 0 \Rightarrow C = 0, \quad (49)$$

$$\vec{E}_z(x, y, c) = 0 \Rightarrow k_z c = p_{1,2,3,\dots} \pi \Rightarrow k_z = \frac{p\pi}{c}. \quad (50)$$

The TE and TM modes in the rectangular cavity are then

$$\vec{H}_z(x, y, z) = H_0 \cos \frac{m\pi x}{a} \cos \frac{n\pi y}{b} \sin \frac{p\pi z}{c} \quad (\text{TE}_{mnp} \text{ modes}), \quad (51)$$

$$\vec{E}_z(x, y, z) = E_0 \sin \frac{m\pi x}{a} \sin \frac{n\pi y}{b} \cos \frac{p\pi z}{c} \quad (\text{TM}_{mnp} \text{ modes}). \quad (52)$$

The resonant frequency associated with the TE_{mnp} or TM_{mnp} mode is found from the separation equation to be

$$k = \omega \sqrt{\mu\epsilon} = 2\pi f_{\text{resonant}} \sqrt{\mu\epsilon} = \sqrt{k_x^2 + k_y^2 + k_z^2} = \sqrt{\left(\frac{m\pi}{a}\right)^2 + \left(\frac{n\pi}{b}\right)^2 + \left(\frac{p\pi}{c}\right)^2}, \quad (53)$$

$$f_{\text{resonant}} = \frac{1}{2\sqrt{\mu\epsilon}} \sqrt{\left(\frac{m\pi}{a}\right)^2 + \left(\frac{n\pi}{b}\right)^2 + \left(\frac{p\pi}{c}\right)^2}. \quad (54)$$

The quality factor (Q) of a waveguide resonator is defined the same way as that

for an RLC network.

$$Q = 2\pi \frac{\text{energy_stored / cycle}}{\text{energy_lost / cycle}} = 2\pi f_{\text{resonant}} \frac{\text{energy_stored}}{\text{power_lost}}, \quad (55)$$

where the energy lost per cycle is that energy dissipated in the form of heat in the waveguide dielectric and the cavity walls (ohmic losses). The resonator quality factor is inversely proportional to its bandwidth as

$$Q = \frac{f_{\text{resonant}}}{\Delta f_{3dB_bandwidth}}. \quad (56)$$

Given a resonator made from a conductor such as copper or aluminum, the ohmic losses are very small and the quality factor is large (high Q, small bandwidth). Thus, resonators are used in applications such as oscillators, filters, and tuned amplifiers. Comparing the modes of the rectangular resonator with the propagating modes in the rectangular waveguide, we see that the waveguide modes exist over a wide band (the rectangular waveguide acts like a high-pass filter) while the rectangular resonator modes exist over a very narrow band (the rectangular resonator acts like a band-pass filter).

In the past, many researchers have reported the theoretical [14-16] and experimental [17-26] results of the cavity perturbation techniques. The measurements of permittivity and permeability of the dielectric materials are performed by inserting a small and appropriately shaped sample into a cavity from a pinhole or longitudinal slot and determining the properties of the sample from the resultant change in the resonant

frequency and loaded quality factor of the cavity. The basic idea of the cavity perturbation is the change in the overall geometric configuration of the electromagnetic fields with the insertion of a small sample must be small. Based on this assumption, a detailed derivation of the perturbation equation for the frequency shift upon the insertion of a sample into a cavity was given by Harrington [27].

In practice, most cavity measurements are also subject to certain pitfalls. The thin material must be self-supporting or supported in the proper place within the cavity. Typically, this is done with some low permittivity material such as foam or Teflon, whose effects must usually be calibrated out. This introduces sources of error to the measurement if the cavity is not assembled in exactly the same way for both the sample-loaded measurement and the unloaded reference measurement (i.e., with and without the thin material of interest). Problems can arise if the sample holder shifts position or a fastening bolt has even slightly different tension on it. Even the process of handling the cavity may cause temperature variations which could affect the geometry enough to be significant to the measurement, which requires measuring frequency shifts well under 1%.

To solve this problem, a novel slotted cavity is employed that allows the sample to be inserted and removed without perturbing the measurement setup. The same waveguide section used in the waveguide method discussed above is used again here with the addition of two coupling irises. Each iris is 0.03" thick and 0.08" radius and serves to

couple energy from WR-90 input waveguide into the dominant TE₁₀₁ mode of the cavity. Two-port measurements were selected over one port because very good signal-to-noise ratio can be obtained in S₂₁ by increasing the input source power. Figure 11 shows the cavity with irises.

From Equation of the cavity resonant frequency, we can observe that the change of dielectric permittivity and magnetic permeability will lead the resonant frequency changing.

In the unperturbed state, the empty cavity, let the electric and magnetic fields in the cavity be

$$\begin{aligned} E &= E_0 e^{j\omega t} \\ H &= H_0 e^{j\omega t} \end{aligned} \quad (57)$$

where E₀ and H₀ are functions of position. When a small piece of sample is inserted into the cavity, the new field distribution and frequency can be modified as,

$$\begin{aligned} E' &= (E_0 + E_1) e^{j(\omega + \delta\omega)t} \\ H' &= (H_0 + H_1) e^{j(\omega + \delta\omega)t} \end{aligned} \quad (58)$$

where E' and H' are the new field, $\delta\omega$ is the shift of frequency. E₁ and H₁ are additional fields which are small comparing to original fields E₀ and H₀. Applying the Maxwell equation,

$$\nabla \times E = -\frac{\partial B}{\partial t} \quad (59)$$

$$\nabla \times H = \frac{\partial D}{\partial t} . \quad (60)$$

substituting the perturbed fields in to above Maxwell equations,

$$\begin{aligned} \nabla \times E_0 &= -\frac{\partial B_0}{\partial t} = -j\omega B_0 \\ \nabla \times (E_0 + E_1) &= -j(\omega + \delta\omega)(B_0 + B_1) . \\ \nabla \times E_1 &= -j[\omega B_1 + \delta\omega(B_0 + B_1)] \\ \nabla \times H_1 &= -j[\omega D_1 + \delta\omega(D_0 + D_1)] \end{aligned} \quad (61)$$

By combining the original E_0 and H_0 with above equations,

$$\begin{aligned} E_0 \cdot \nabla \times H_1 + H_0 \cdot \nabla \times E_1 = \\ j\omega[E_0 \cdot D_1 - H_0 \cdot B_1] + j\delta\omega[(E_0 \cdot D_0 - H_0 \cdot B_0) + (E_0 \cdot D_1 - H_0 \cdot B_1)] . \end{aligned} \quad (62)$$

Here, we have

$$\begin{aligned} B_0 &= \mu_0 H_0 \\ B_1 &= \mu_0 H_1 \\ D_0 &= \varepsilon_0 E_0 \\ D_1 &= \varepsilon_0 E_1 \end{aligned} \quad (63)$$

outside the sample. And inside the sample, the relation of field and flux is

$$D_1 = \varepsilon_0[\varepsilon_r(E_0 + E_1) - E_0] ,$$

$$B_1 = \mu_0[\mu_r(H_0 + H_1) - H_0] \text{ for isotropic material.}$$

Use the vector identity

$$\nabla \cdot [(H_0 \times E_1) + (E_0 \times H_1)] \equiv E_1 \cdot \nabla \times H_0 - H_0 \cdot \nabla \times E_1 + H_1 \cdot \nabla \times E_0 - E_0 \cdot \nabla \times H_1 , (63)$$

$$H_0 \cdot \nabla \times E_1 + E_0 \cdot \nabla \times H_1 = j\omega(E_1 \cdot D_0 - H_1 \cdot B_0) - \nabla \cdot [(H_0 \times E_1) + (E_0 \times H_1)] . (64)$$

By some mathematic manipulations, we obtain

$$\begin{aligned}
& j\omega(E_1 \cdot D_0 - H_1 \cdot B_0) - \nabla \cdot [(H_0 \times E_1) + (E_0 \times H_1)] = \\
& j\omega[E_0 \cdot D_1 - H_0 \cdot B_1] + j\delta\omega[(E_0 \cdot D_0 - H_0 \cdot B_0) + (E_0 \cdot D_1 - H_0 \cdot B_1)] \quad (65)
\end{aligned}$$

Let V_0 be the volume of the cavity and V_1 the volume of the sample. Thus $V_0 - V_1$ is the part of the cavity not occupied by the sample. Integrate over the volume V_0 :

$$\begin{aligned}
& j\omega \iiint_{V_0} (E_1 \cdot D_0 - H_1 \cdot B_0) dV - \iiint_{V_0} \nabla \cdot [(H_0 \times E_1) + (E_0 \times H_1)] dV = \\
& j\omega \iiint_{V_0} (E_0 \cdot D_1 - H_0 \cdot B_1) dV + j\delta\omega \iiint_{V_0} [(E_0 \cdot D_0 - H_0 \cdot B_0) + (E_0 \cdot D_1 - H_0 \cdot B_1)] dV \quad (66)
\end{aligned}$$

By Green's theorem,

$$\iiint_{V_0} \nabla \cdot [(H_0 \times E_1) + (E_0 \times H_1)] dV = \iint_S [(H_0 \times E_1) + (E_0 \times H_1)] \cdot \hat{n} dS \quad (67)$$

The direction of cross product of electric field and magnetic field ($H_0 \times E_1$) and ($E_0 \times H_1$) is tangential to the walls. So their dot product with \hat{n} is zero.

By assumption that $\delta\omega \ll \omega$, E_1 and H_1 are smaller than E_0 and H_0 over the entire cavity, we can simplify the integral to

$$\begin{aligned}
& j\omega \iiint_{V_1} (E_1 \cdot D_0 - H_1 \cdot B_0) dV = \\
& j\omega \iiint_{V_1} (E_0 \cdot D_1 - H_0 \cdot B_1) dV + j\delta\omega \iiint_{V_0} (E_0 \cdot D_0 - H_0 \cdot B_0) dV \quad (68)
\end{aligned}$$

The frequency shift can be presented by

$$\frac{\delta\omega}{\omega} = \frac{\iiint_{V_1} (E_1 \cdot D_0 - H_1 \cdot B_0) - (E_0 \cdot D_1 - H_0 \cdot B_1) dV}{\iiint_{V_0} (E_0 \cdot D_0 - H_0 \cdot B_0) dV} \quad (69)$$

If we consider the complex permittivity, permeability and complex fields, the variation of resonance frequency is given by [21] as

$$\frac{f - f_0}{f} = - \frac{\int (\Delta \hat{\varepsilon} E \cdot E_0 + \Delta \hat{\mu} H \cdot H_0) dv}{\int (\varepsilon E \cdot E_0 + \mu H \cdot H_0) dv}, \quad (70)$$

where ε and μ are the permittivity and permeability of the medium in the unperturbed cavity. dv is the elementary volume and $\Delta\varepsilon$ and $\Delta\mu$ are the changes in the permittivity and permeability due to the introduction of the sample in the cavity. Without affecting the generality of Maxwell's equations, the complex frequency shift due to lossy sample in the cavity is given as

$$-\frac{df}{\hat{f}} = \frac{(\hat{\varepsilon}_r - 1) \varepsilon_0 \int_{v_s} \hat{E} \cdot \hat{E}_0^* dv + (\hat{\mu}_r - 1) \mu_0 \int_{v_s} \hat{H} \cdot \hat{H}_0^* dv}{\int_{v_c} (\hat{D}_0 \cdot \hat{E}_0^* + \hat{B}_0 \cdot \hat{H}_0^*) dv}, \quad (71)$$

where $d\hat{f}$ is the complex frequency shift because the permittivity of practical materials is complex. B_0 , H_0 , D_0 and E_0 are the fields in the unperturbed cavity and E and H is the field in the inserted thin film samples.

In terms of energy, the numerator of equation (71) represents the energy stored in the sample and the denominator represents the total energy stored in the cavity. The total energy $W = W_e + W_m$ where W_e and W_m are the electric and magnetic energy, respectively. With the aforementioned assumptions applied on equation (71), the fields in the empty part of the cavity are negligible changed by the insertion of the sample. The fields in the sample are uniform over its volume. Both of these assumptions can be considered valid if the sample is sufficiently small relative to the resonant wavelength. The negative sign in equation (71) indicates that by introducing the sample, the resonance

frequency is lowered. When a dielectric sample is inserted into the cavity resonator where the maximum perturbation occurs that is at the position of maximum electric field, only the first term in the numerator is significant, since a small change in ϵ_r at a point of zero electric field or a small change in μ_r at a point of zero magnetic field does not change the resonance frequency. The transverse slotted cavity is working in TE_{101} mode, the distribution of the magnitude of electric fields and magnetic fields is shown in Figure 14.

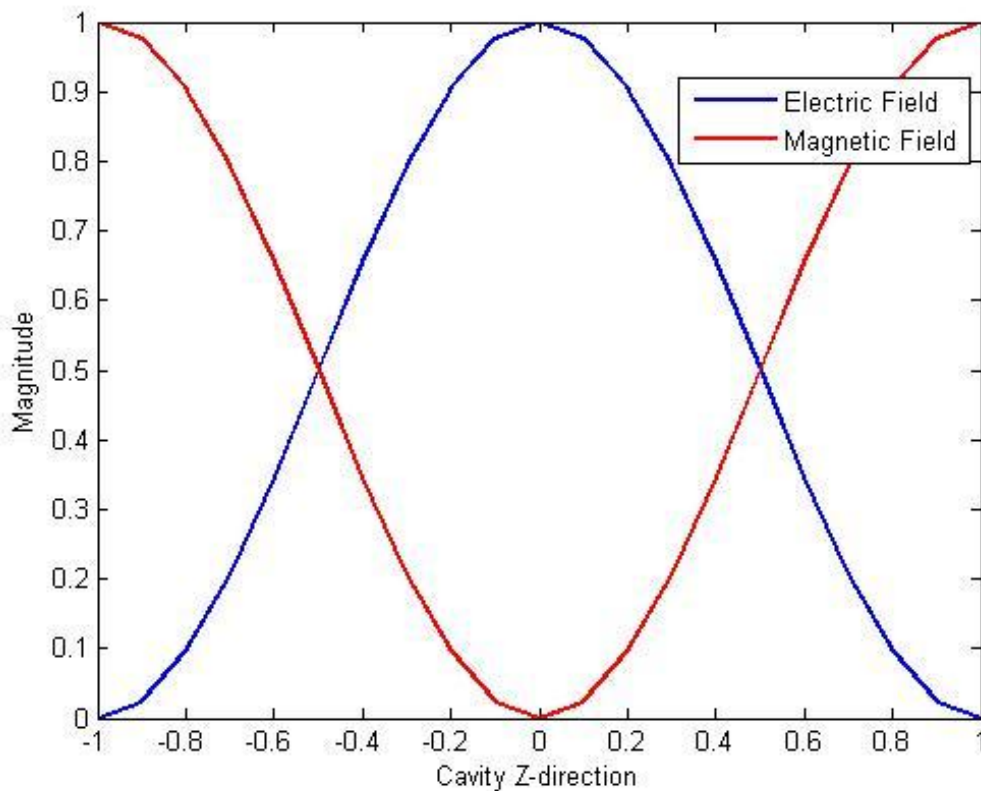


Figure 14: Schematic curves of magnitude of electric field and magnetic field.

The transverse slot is located at the center of the z-direction. Thus the sample is inserted at the position of maximum electric field and zero magnetic field. Therefore

Equation (71) can be reduced to

$$-\frac{d\hat{f}}{\hat{f}} = \frac{(\hat{\epsilon}_r - 1) \int_{v_s}^{\hat{E} \cdot \hat{E}_{0\max}^* dv}{2 \int_{v_c} |E|^2 dv}}{2 \int_{v_c} |E|^2 dv}. \quad (72)$$

Thin film sample of complex permittivity $\hat{\epsilon}_r = \epsilon' + j\epsilon''$ is kept at the maximum electric field location of the cavity. The thin film sample is inserted and taken the entire transverse section of the cavity. After the introduction of the sample the empty resonant frequency and Q-factor alter, due to the change in the overall capacitance and conductance of the cavity. If f_0 and Q_0 are the resonance frequency and quality factor of the cavity without sample and f and Q all the corresponding parameters of the cavity loaded with the sample. The complex resonant frequency shift is related to measurable quantities by

$$\frac{d\hat{f}}{\hat{f}} = \frac{f - f_0}{f_0} + \frac{j}{2} \left(\frac{1}{Q} - \frac{1}{Q_0} \right). \quad (73)$$

Thus we can integrate the integral of electric field and get the relation of the real part of complex permittivity and resonant frequency as

$$\frac{f - f_0}{f_0} = -\frac{(\epsilon' - 1)abt}{abc} \quad (74)$$

where a, b and c are dimension of the cavity, t is the thickness of the thin film sample.

Then the real part of permittivity is determined by

$$\varepsilon' = 1 + \left(1 - \frac{f}{f_0}\right) \frac{c}{t}. \quad (75)$$

Similarly, the imaginary part of complex permittivity can be got by substitute the imaginary part of Equation (73) to Equation (72).

$$\varepsilon'' = \frac{1}{2} \left(\frac{1}{Q} - \frac{1}{Q_0} \right) \frac{c}{t}. \quad (76)$$

The Agilent 8510C vector network analyzer is used to make the slotted cavity measurement. Figure 12 shows the special slotted cavity setup. The thin films can be placed inside the waveguide. TRL calibration was used in order to minimize the systematic errors in the measurement process. The advantage of a transverse slotted cavity for X band connected at the other port to measure the thin films was also utilized here. The transverse slotted waveguide method is a novel technique and a number of known samples such as Teflon, Mylar, and black polyester are measured for validation of this new technique. The resonance frequency of the TE₁₀₁ mode in the sample-loaded cavity was measured using the vector network analyzer and this was used to calculate the real part of the specimen permittivity. Plots of S₂₁ showing the resonant shift due to the addition of the Teflon sample are shown in Figure 15.

The results for the 8.8 GHz dominant mode are shown in Table I for 1 mil thick samples of Teflon, black polyester, and black Kapton. Coupling is typically -50 dB, and Q values are typically 2500. Excellent agreement is obtained with the known permittivity

of Teflon (between 2 and 2.1). This validates the sensitivity of the technique. Performing the measurements more than once indicated the results were repeatable to less than 1% precision.

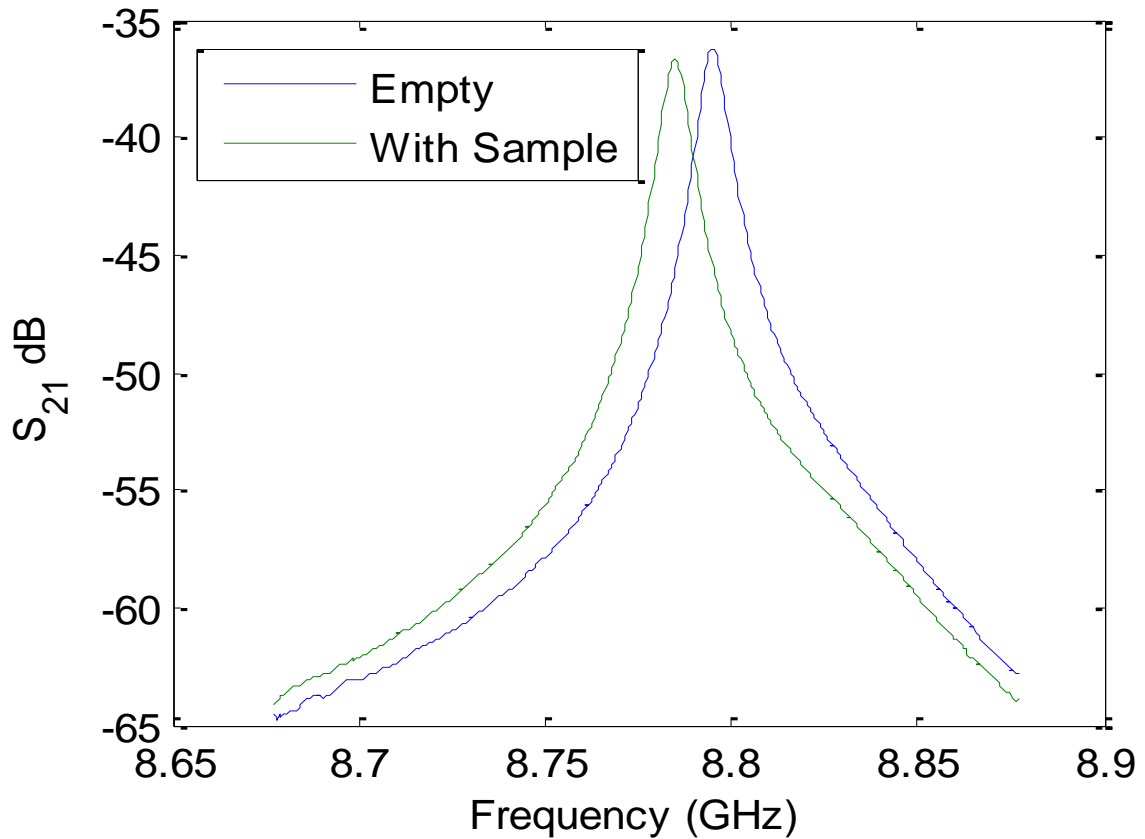


Figure 15: Measured S_{21} of Slotted Cavity With and Without Teflon Sample showing the resonant frequencies.

Table 2 Measured Relative Permittivity of Several Thin Film Materials Using a Slotted Cavity

Material	Real Permittivity ϵ'
Teflon	2.07

Black Polyester	3.05
Black Kapton	8.07

2.8 Measurement Results

Teflon, Mylar polyester, and black polyester thin films were chosen to investigate the validity of these newly developed techniques at the beginning. The thicknesses of each sample ranged from 1 mil (25.4 μm) to 0.5 mil (12.7 μm). The experiment was conducted with a single layer of the thin film as well as with multiple layers of the same sheet of thin film to observe the variation of the real part of permittivity value with increasing total thickness of the stacked material. The measurement was then extended for several other thin film materials. Tables below show the resonant frequency and the real part of permittivity values for different numbers of layers of thin films for Teflon, black polyester with different film thicknesses, Mylar, polyphenylene sulfide, fluoropolymer, polyethylene with different film thicknesses, and acetal polyoxymethylene. The resonant frequency decreases with increasing layers of thin film stacked inside the slotted cavity. The real part of the permittivity values seem to be consistent and the variation does fall within the random error limit. Data for a total of eleven different thin film samples measured with the new slotted cavity are presented.

Table 3 Relative Permittivity of Teflon (thickness = 0.001 inch)

Number of Layers	Resonant Frequency (GHz)	Permittivity
1	8.7965	2.0788
2	8.7865	2.1072
3	8.7767	2.1091
4	8.7677	2.087
5	8.7577	2.097

The permittivity of Teflon is known to be close to 2.1. The values obtained from the measurements are close to 2.1.

Table 4 Relative Permittivity of Black Polyester (thickness = 0.001 inch)

Number of Layers	Resonant Frequency (GHz)	Permittivity
1	8.7885	2.9873
2	8.7708	2.9986
3	8.753	3.0062
4	8.735	3.0157
5	8.7117	3.1417

Table 5 Relative Permittivity of Mylar Polyester Film (thickness = 0.001 inch)

Number of Layers	Resonant	Permittivity
-------------------------	-----------------	---------------------

Frequency (GHz)		
1	8.7888	2.953214
2	8.7721	2.924824
3	8.7554	2.915361
4	8.7379	2.933341
5	8.7212	2.92596

Dielectric constant of Mylar has been published to be 2.8-3.2 depending on the frequency from DuPont product sheet.

Table 6 Relative Permittivity of Polyphenylene Sulfide (thickness = 0.003 inch)

Number of Layers	Resonant Frequency (GHz)	Permittivity
1	8.7554	2.915361
2	8.7029	2.951321
3	8.6512	2.953214

Reference from industrial data sheet: Dielectric constant at 1 GHz is 3.3.

Table 7 Relative Permittivity of Fluoropolymer Film (thickness = 0.001 inch)

Number of Layers	Resonant Frequency (GHz)	Permittivity
1	8.7988	1.817624
2	8.7899	1.914149
3	8.7814	1.931183

4	8.7736	1.919827
5	8.7659	1.910743

Table 8 Relative Permittivity of Polyethylene Film (thickness = 0.003 inch)

Number of Layers	Resonant Frequency (GHz)	Permittivity
1	8.7751	2.169657
2	8.7429	2.194261
3	8.7106	2.203725

Table 9 Relative Permittivity of Polyethylene Film (thickness = 0.005 inch)

Number of Layers	Resonant Frequency (GHz)	Permittivity
1	8.7521	2.224165
2	8.6981	2.225301

Known permittivity value = 2.26.

Table 10 Relative Permittivity of Acetal Polyoxymethylene Film (thickness = 0.003 inch)

Number of Layers	Resonant Frequency (GHz)	Permittivity
1	8.7575	2.835869
2	8.7019	2.970248

3	8.6585	2.861105
---	--------	----------

Table 11 Relative Permittivity of Black Polyester (thickness = 0.001 inch)

Number of Layers	Resonant Frequency (GHz)	Permittivity
1	8.79156	3.028508

Table 12 Relative Permittivity of Black Polyester (thickness = 0.00075 inch)

Number of Layers	Resonant Frequency (GHz)	Permittivity
1	8.7930	3.486729
2	8.77648	3.49354
3	8.7600	3.493792
4	8.7437	3.487108

Above two black polyesters do not have same composite.

3. Dielectric Permittivity Measurement at Terahertz Frequency

3.1 Introduction

In physics, terahertz radiation comprises electromagnetic waves propagating at frequencies in the terahertz range, from 0.3 to 3 THz. Operationally, terahertz radiation becomes of interest because it approximately represents the region in the electromagnetic spectrum that the frequency of electromagnetic radiation ceases to be measured directly, and must be measured only by the proxy properties of wavelength and energy. For related reasons, terahertz radiation also represents the region in which the generation and modulation of coherent electromagnetic signals ceases to be possible by the conventional means used to generate most coherent radio waves and microwaves, and requires new devices and techniques, many of which are novel. Both thin film materials and terahertz radiation are pretty useful especially in astronomy.

THz radiation has several distinct advantages over other forms of spectroscopy: many materials are transparent to THz, THz radiation is safe for biological tissues because it is non-ionizing (unlike for example X-rays), and images formed with terahertz radiation can have relatively good resolution (less than 1 mm). Also, many interesting materials have unique spectral fingerprints in the terahertz range, which means that terahertz radiation can be used to identify them.

Usually, people use time domain terahertz spectroscopy or Fourier transform

spectroscopy to characterize materials in terahertz frequencies. In this dissertation, dispersive Fourier transform spectroscopy is employed to determine the complex permittivity of thin film materials.

3.2 Dispersive Fourier Transform Spectroscopy

Fourier spectroscopy has proven to be a viable method for broadband measurement of materials. In dispersive Fourier transform spectroscopy (DFTS), a spectrum is constructed by performing a numerical Fourier transform in the digitized interference pattern, recorded as a function of path difference within the interferometer. This allowed the continuous spectrum for absorption and refraction to be mapped at any resolution over the entire millimeter, far-infrared, and mid-infrared region, hence linking the microwave world with mid- and near-infrared world.

Fourier spectrometers offered many advantages over the hugely popular grating spectrometers, in that they give both absorption and refraction data. Also, the optical and mechanical requirements of the Fourier spectrometer systems were less strict than those of the grating systems. Initially, the Fourier spectrometers were very successful in many areas that dealt with physics and chemistry; however, like the grating spectrometer, it could only provide absorption and refraction data at first. After some time, the need for a machine setup to provide a direct route to the absorption, refraction, and especially the permittivity data for frequencies above 30 GHz became evident.

The interferogram of a sample is measured and compared to a reference. It introduces a phase shift in addition to the amplitude loss. The dielectric properties of the sample shift and distort the interferogram signature. Using a double-sided complex Fourier transform, the phase and modulus spectra of the sample in question are produced. These data, along with a comparison to the reference interferogram, can be used to derive the refractive index and the real part of complex dielectric permittivity of the sample [5]. The technique was implemented for various materials such as solids, liquids, gases, magnetic materials, powders, composites, biological specimens, and materials at low and high temperatures. This technique can now be used routinely at our labs at Tufts University at millimeter waves (even as long as 10 mm) as well as submillimeter and mid-infrared frequencies for the measurement of spectra for absorption coefficient, refractive index, real and imaginary parts of complex permittivity, and loss tangent with unprecedented precision. Dispersive Fourier transform spectroscopy can also be used for the measurement of real and imaginary parts of complex magnetic permeability of ferrites and magnetic materials [6].

An improvement on the active arm was made so the scanning mirror can now move in 500 nano meter steps. The resolution of the dispersive Fourier transform spectroscopy was improved to a higher stage. DFTS provides a broadband measurement of the permittivity of a sample at frequencies much higher than those measured in slotted-cavity methods. Thus, successfully applying DFTS methods to low-loss thin film materials is expedient.

In a dispersive Fourier transform Spectroscopy (DFTS), the thin film sample rests in one the mirror arm of a two beam interferometer to provide the phase information in addition to the amplitude information. This leads to the determination of both the real and imaginary parts of complex dielectric permittivity as a continuous function of frequency. The newly improved DFTS setup consists of a 1000 step micromotor per rotation (0.5 mm) for the scanning mirror arm, oscillators, a lock-in amplifier, power supply, and an ultrasensitive liquid-helium-cooled InSb hot-electron-effect bolometer detector. The interferometer was optically and electronically tuned to ensure a maximum signal and a good signal to noise ratio. A 125 Watts quartz-encapsulated mercury vapor lamp is used to generate the broadband radiation. It is necessary to employ an ultra sensitive liquid helium cooled indium antimonide detector at millimeter and sub-millimeter wave frequencies as the energy from the lamp is low over such wide frequency band. The millimeter wave free carrier absorption of the semiconductor material becomes an ultra sensitive broadband detector from about 30 GHz to 1000 GHz. The beams from the lamp are collimated using mirrors and directed toward the wire-grid polarizer/analyzer. The use of freestanding wire-grid polarizers as beam splitters eliminates the channel effect at lower frequencies and gives a pass band performance from 60 GHz to a high cutoff frequency at 6 THz. After passing through the polarizer, the radiation is divided into two branches with a beam splitter. One component travels to a scanning mirror, and the other part passes through a Mylar window before reaching the thin film sample. After traversing through the thin film sample, a fixed mirror reflects the radiation back toward

the beam splitter grid. The scanning mirror's motion is carefully controlled using a micrometer and micromotor. Each sampling period is set to 0.5 s to make sure the micromotor and the scanning mirror is not vibrating. The radiation that reaches the scanning mirror is phase modulated through a 45° mirror. After reflecting from the fixed and scanning mirrors, the two radiation branches recombine, yielding an interferogram.

The thermal and mechanical stabilities of interferometer components are very important for the low-frequency performance. Water-cooling units control the interferometer temperature with an accuracy of ± 0.1 °C. Tubes extend from the cooling units to all parts of the interferometer. Strong conducting metal contact plates are used to ensure that the regulated temperature from the tubes is transferred to the components. The most vital part of the interferometer that needs cooling is where the radiation enters. As the mercury lamp has a power of 125 Watts, this entry point gets heated the most and can easily get damaged if adequate cooling is not provided. The system temperature can be adjusted by digitally setting the cooling units to the desired temperature, thus allowing variable temperature measurements in this setup.

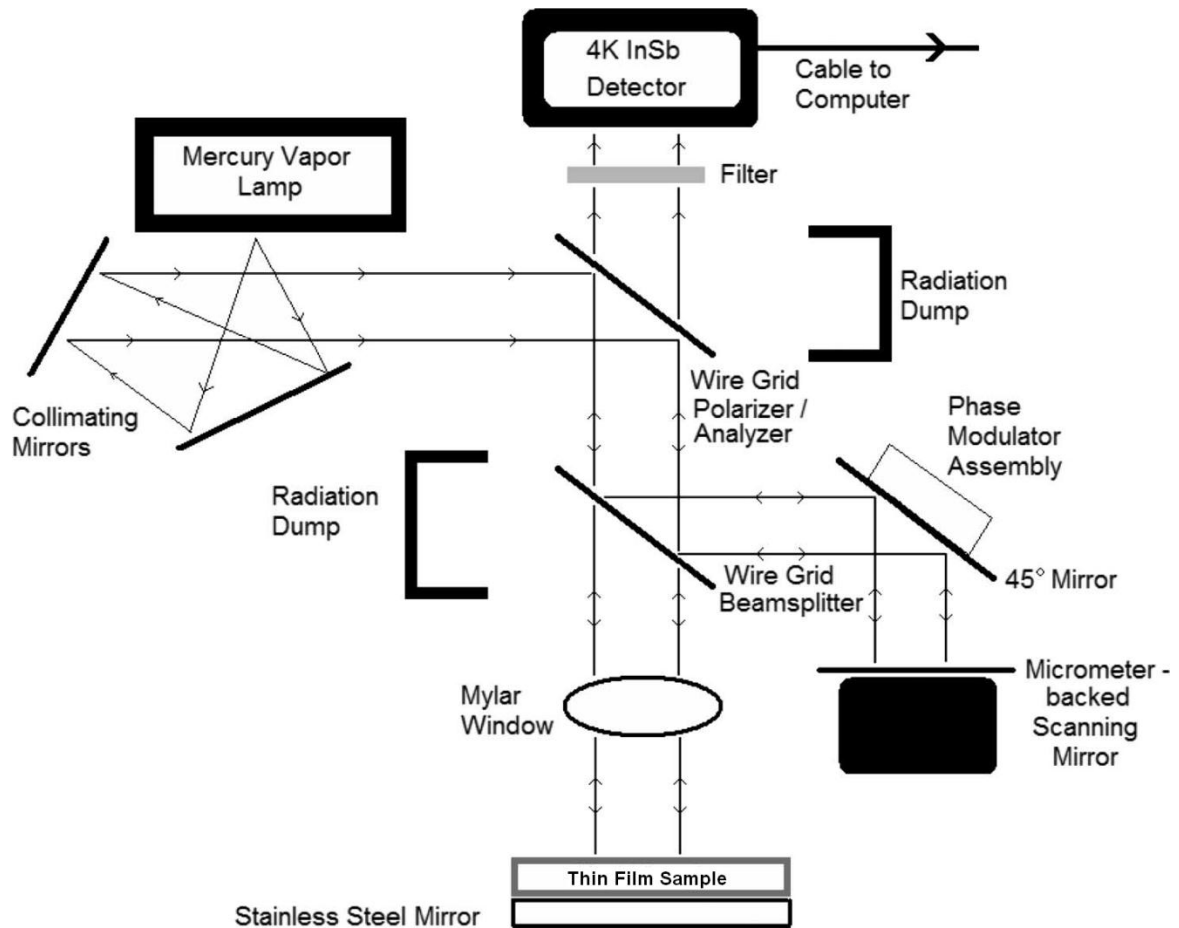


Figure 16: Ray diagram of the dispersive Fourier transform interferometer. The beam division is accomplished by using a pair of free standing wire grid polarizers. One grid acts as a polarizer/analyzer and other grid as a beam divider and beam recombiner. Note that the specimen rests in one of the active mirror arm of the interferometer to provide the phase information in addition to the amplitude information.

Figure 16 shows a line diagram of the dispersive Fourier transform spectrometer. To get enough sensitivity, an improvement of 500 nano-meter step size is successfully achieved on the scanning mirror movement for the first time. It thus provided us with highly resolved phase information. This high resolution phase information lead us to

determine the real part of complex dielectric permittivity of one mil (25.4 μm) thickness thin films very accurately from 60 GHz to 1000 GHz.

Once the two interference patterns, shift, and sample thickness are known, multiple reflection signatures can be edited out, and a double-sided Fourier transform of the interferograms is performed to yield more stable phase information in the frequency domain. One can then proceed to calculate the five optical and dielectric parameters investigated in this paper namely the absorption coefficient, the refractive index, the real and imaginary part of complex dielectric permittivity and the loss tangent. The refractive index is found by

$$n(\tilde{\nu}) = 1 + \frac{x}{d_s} + \frac{ph\{S_T(\tilde{\nu})\} - ph\{S_o(\tilde{\nu})\} - ph\{(S'(\tilde{\nu}))^2\}}{4\pi\tilde{\nu}d_s}, \quad (77)$$

where x is the shift, d_s is the sample thickness, $\tilde{\nu}$ is the wave number per cm, the wave number is related to frequency ν via c , the speed of light, and $ph\{\}$ indicates the phase of the contents within the parentheses. $S_T(\tilde{\nu})$ and $S_o(\tilde{\nu})$ are the Fourier transforms of the edited sample and reference interference pattern. $S'(\tilde{\nu})$ is derived from the ratio of $S_T(\tilde{\nu})$ and $S_o(\tilde{\nu})$. Similarly, the absorption coefficient can be found by

$$\alpha(\tilde{\nu}) = \frac{1}{d_s} \left[\ln \frac{S_o(\tilde{\nu})}{S_T(\tilde{\nu})} + \ln(S'(\tilde{\nu}))^2 \right]. \quad (78)$$

From Maxwell's Equation, the complex refractive index $n(\tilde{\nu})$ is defined as,

$$\hat{n}(\tilde{\nu}) = n(\tilde{\nu}) - i \frac{\alpha(\tilde{\nu})}{4\pi\tilde{\nu}}. \quad (79)$$

Then the complex permittivity and loss tangent can be calculated from the complex refractive index,

$$\varepsilon(\tilde{\nu}) = \{n(\tilde{\nu})\}^2 = \varepsilon'(\tilde{\nu}) - i\varepsilon''(\tilde{\nu}), \quad (80)$$

$$\tan \delta = \frac{\varepsilon''(\tilde{\nu})}{\varepsilon'(\tilde{\nu})}. \quad (81)$$

Phase modulation is employed by periodically vibrating a mirror in the optical path. The vibration period can be tuned and adjusted depending on the operational frequency and path difference within the interferometer. The system has been designed so that the specimen is placed in one of the active arms. This allows one to acquire the phase as well as amplitude information of the retrieved signal. In this study, we were able to further reduce the step size of the scanning mirror to 500 nanometer. This provides high resolution phase information and hence the accuracy of results increases. The interferometer is placed on a vibration absorbing table to ensure that external vibrations do not affect the system.



Figure 17: Set up for the measurement of thin film samples. The golden cylinder is the bolometer. The solid machine has been leveled to ensure optical alignment of all devices and sample holder.

3.3 Improvement and Results

The key improvement in the dispersive Fourier transform spectroscopy is that the step size of the active mirror movement achieves 500 nanometer. Thus the spectroscopy can record accurate amplitude and phase information of the thin film samples. The traditional dispersive Fourier transform spectroscopy does not have such ability to record accurate phase information for the thin films because the thickness of the thin films

provide very small phase shift.

Commercial available common Teflon, Mylar polyester, and black polyester thin films were chosen to investigate the validity of the newly improved dispersive Fourier transform spectroscopy. The thicknesses of each sample ranged from 1 mil (25.4 μm) to 0.5 mil (12.7 μm). The experiment was conducted with a single layer of the thin film.

At the beginning, a reference measurement without any sample in the sample holder was performed to provide the reference interferogram. Then Teflon, Mylar and black polyester were measured. The reference interferogram and shifted interferogram from 1 mil (26.5 μm) Mylar is shown in Figure 18. Both altitude change and phase change can be observed in the figure. The amplitude and phase information was converted to complex dielectric permittivity later. The shift in the path difference unit is approximately 40 micrometers.

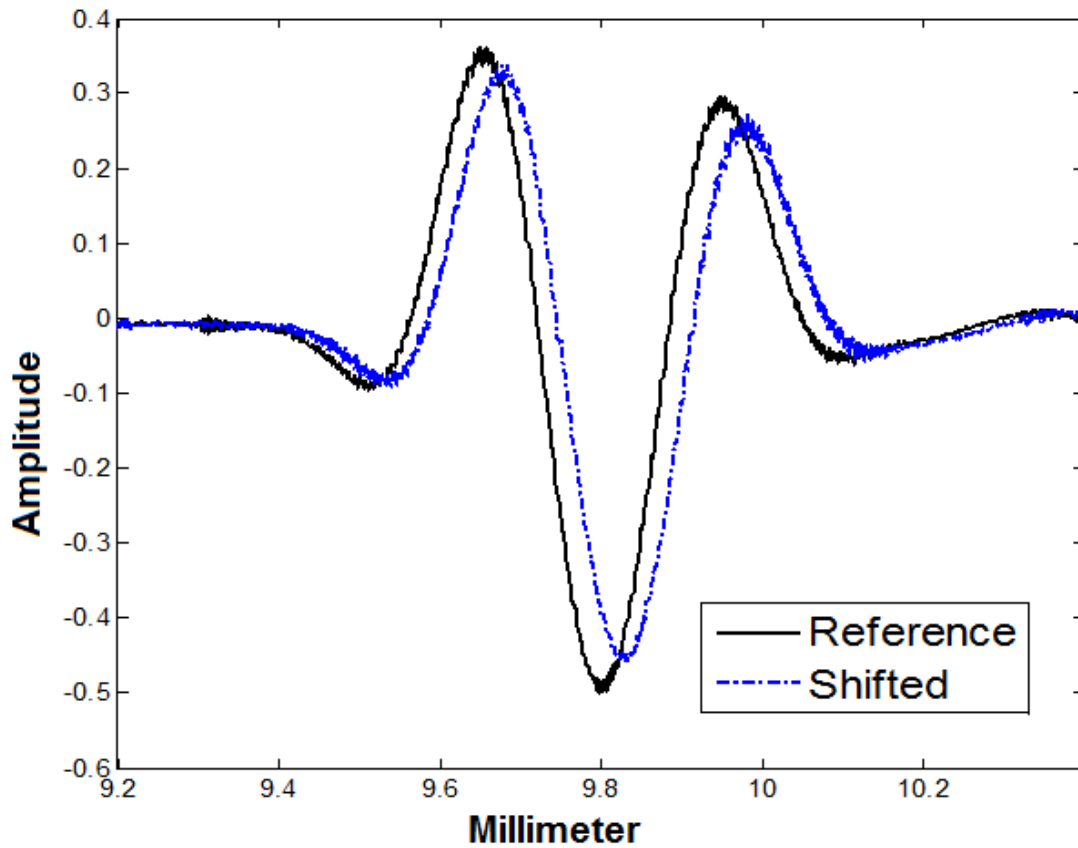


Figure 18: Reference interferogram without any thin film sample and shifted interferogram from Mylar thin film.

Figure 19, 20, 21 show the real part of dielectric permittivity spectra for Teflon, Mylar, and black polyester thin film samples from about 300 GHz to 700 GHz, respectively. For such thin film, small errors can lead to a large error in the calculation of permittivity. The measurement of thickness should be accurate and the film should be smooth without any wrinkle. Although it is difficult to measure the thickness of the thin film accurately, the average values of the real part of dielectric permittivity spectra presented in Figures agree well with previously measured permittivity values of bulk

materials. We have employed a pressure sensitive precision micrometer to measure the film thickness at many positions and an average value was taken. A better idea for measuring the thickness is to measure the total thickness of many layers divided by the total number of layers.

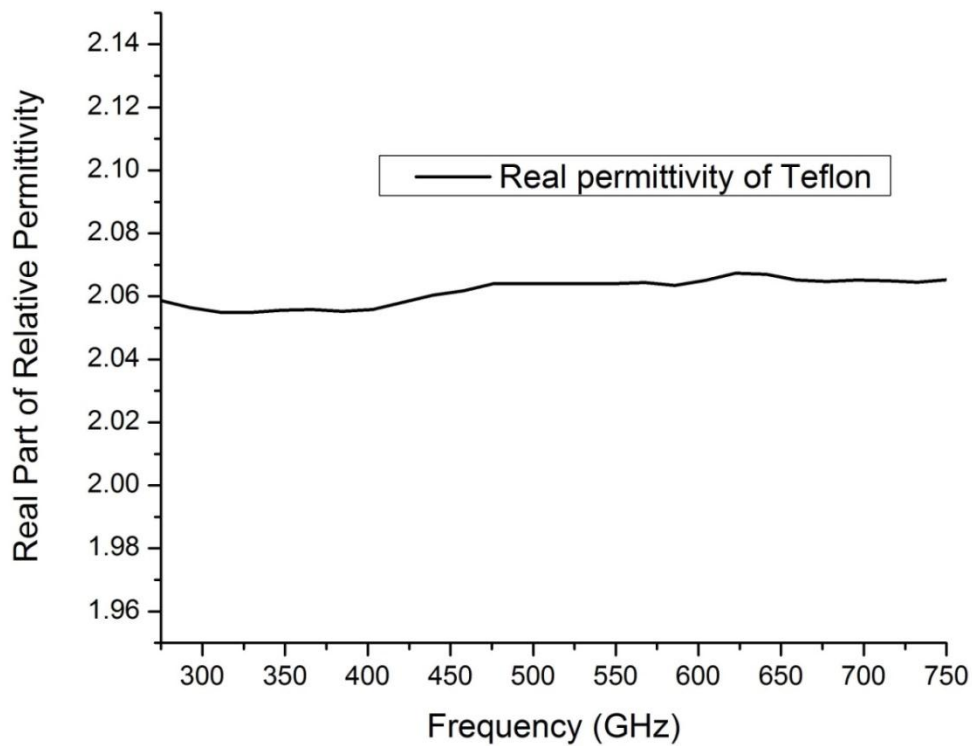


Figure 19: Relative real dielectric permittivity of Teflon thin film with 25.4 um thickness.

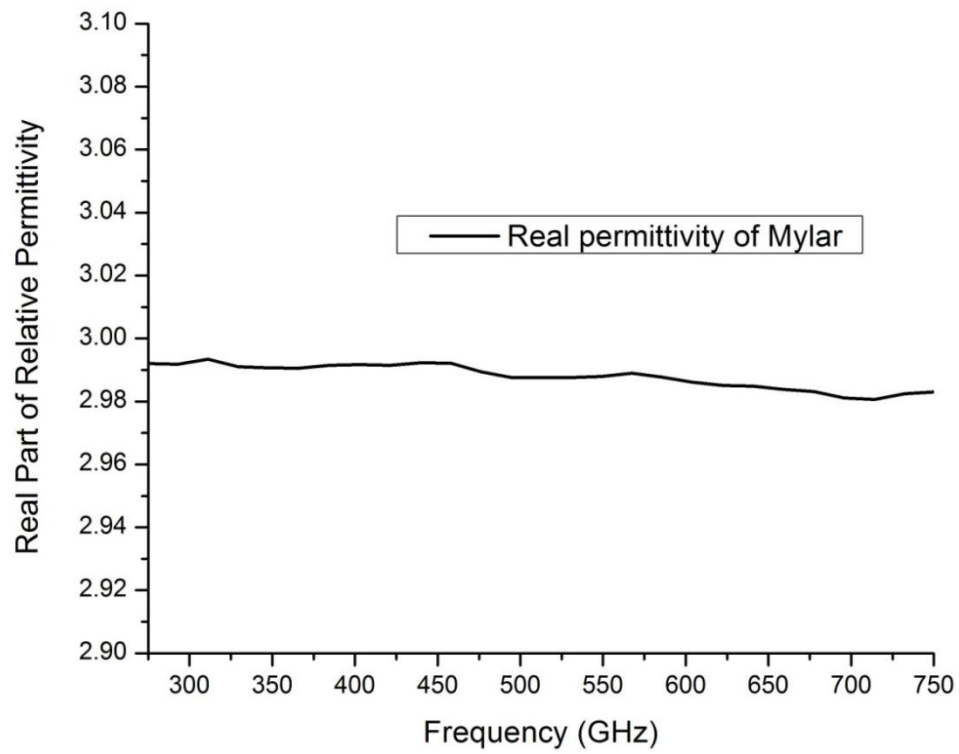


Figure 20: Relative real dielectric permittivity of Mylar thin film with 26.5 um thickness.

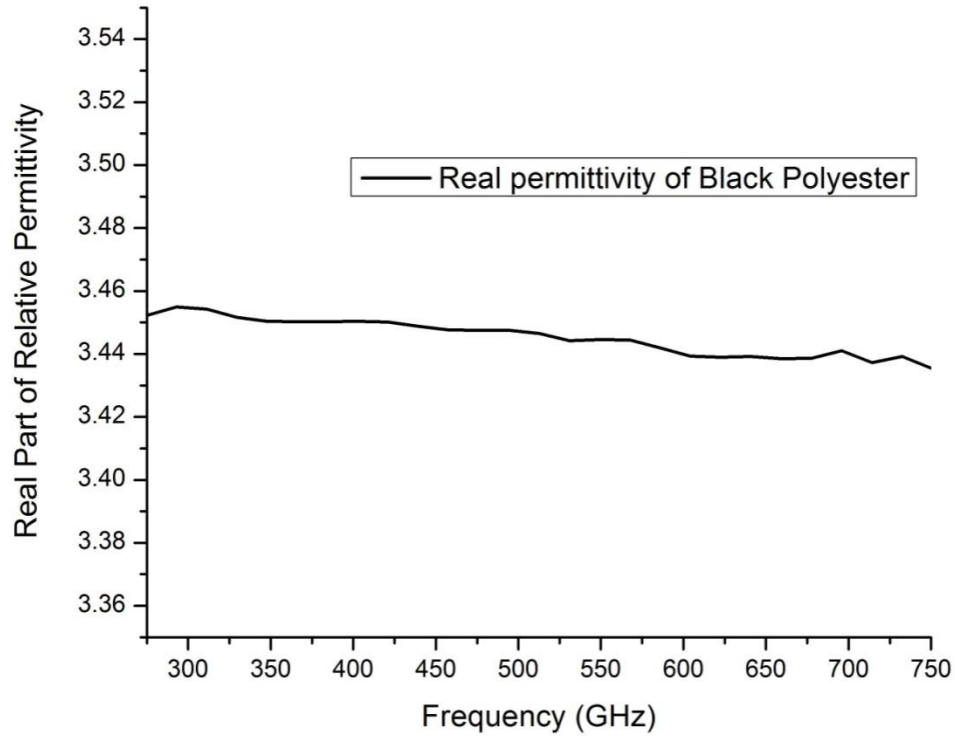


Figure 21: Relative real dielectric permittivity of black polyester thin film with 19 μm thickness.

3.4 Discussion

The spectra of the dielectric permittivity of samples are stable over the frequency though some ripples show. These ripples come from the interference between the thin film reflection and the mirror reflection. The thickness of thin film materials is extremely small, so the shifted interferogram consists of stack of the main reflection from the fixed

mirror and reflection from the thin film surface. Figure 22 shows the sketch of the multiple reflection and possible multiple interference.

Usually, for a low loss thin film sample, energy beam from the source will be reflected at the front surface and back surface shown in Figure 22. These reflections will form a reflected interferogram away from the transmitted interferogram shown in Figure 23. The distance between these two interferograms is $2d+x$, where d is the thickness of the thin film sample and x is the shift of the transmitted interferogram [28]. The distance $2d+x$ results in a small value for the thickness of the thin film sample is so small. Thus the interferograms overlap each other which results in slight difference between measured real permittivity and theoretical value.

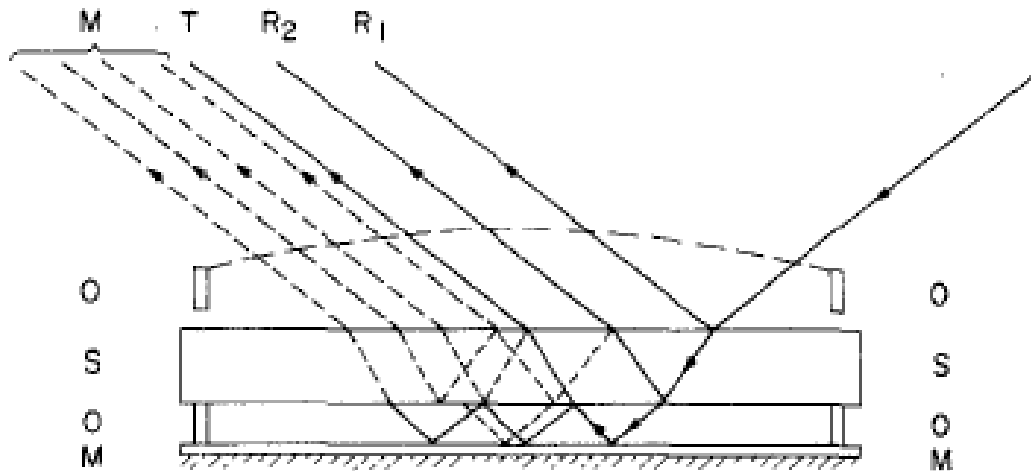


Figure 22: Multi-reflection diagram. O, S, M represent dry air, solid thin film, and mirror, respectively. R1 is the front specimen surface reflected beam, R2 is the back specimen surface reflected beam, T is the transmitted beam, and M are multiply reflected beams. Beams are in normal incidence, but shown at inclined incidence for figure clarity.

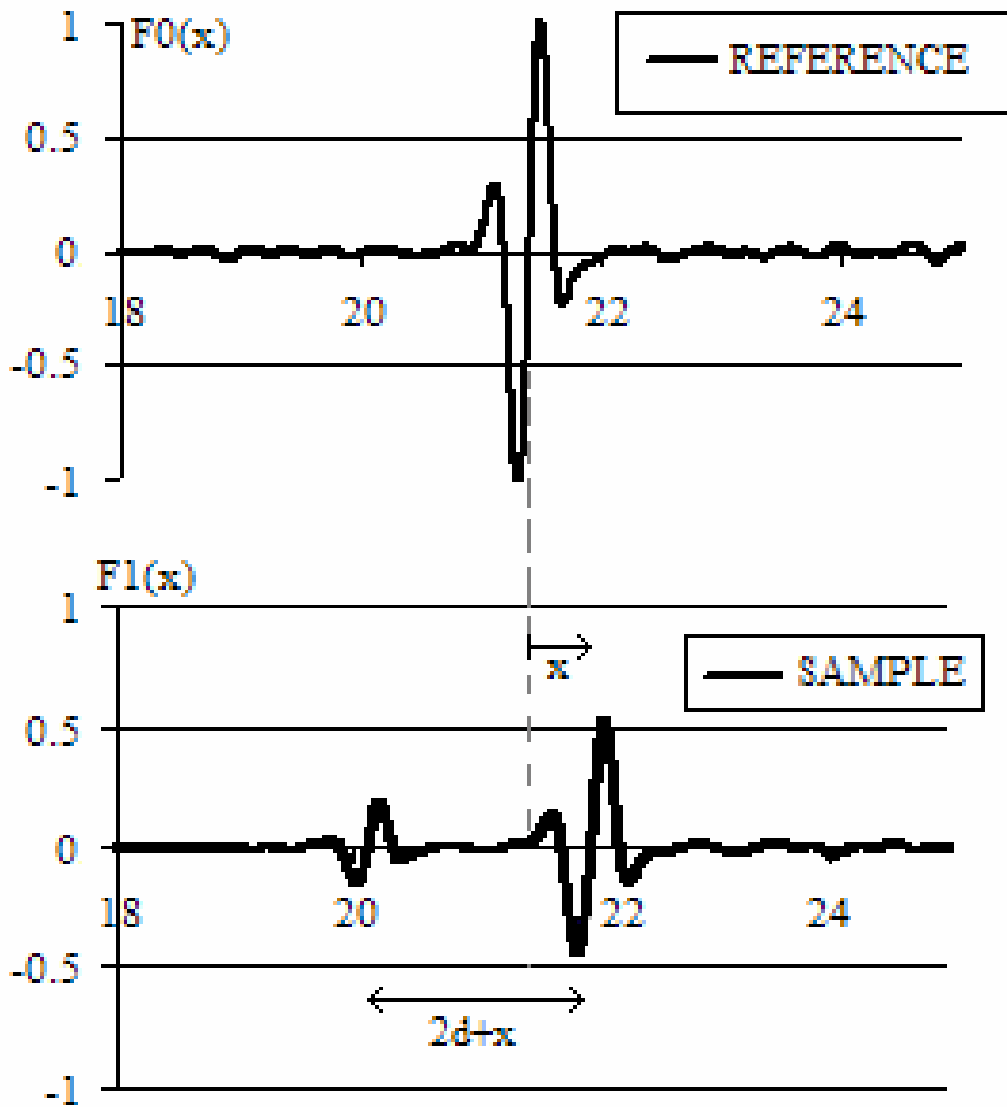


Figure 23: A schematic of the reference and specimen interferograms with multi-reflection. It shows not only one interferogram in the shifted interferogram pattern with sample.

Since the use of infinite interferograms would be impossible, Fourier integrals of truncated weighted interferograms are used instead. Actually, there are two air interfaces

and hence multiple reflections. As the energy from each reflection diminishes quickly. Spectra after second reflection can be ignored as 0 energy. Then the sample interferogram can be represented by the following equation,

$$F_1(x) = F_{R1}(x) + F_{R2}(x) + F_T(x) + F_M(x). \quad (82)$$

In this equation, x is the distance travelled by the scanning mirror, $F_{R1}(x)$ is one of the multiple interferogram signatures that occurs at the top surface of the sample, $F_M(x)$ is for mirror reflection and $F_T(x)$ is the interferogram signature occurring after transmission through the thin film sample and a reflection from the fixed mirror as shown in Figure 23.

A correction method is employed to subtract the reflected interferogram and phase information from the recorded interferogram. In a measurement, an extra measurement without the fixed mirror is taken to get a reflected interferogram. Reflection from the surface of the thin film can be used to yield complex amplitude reflectivity $\hat{r}(\nu)$. The complex refractive index $n(\nu)$ can then be found directly at each value of ν from $\hat{r}(\nu)$ which is related to $\hat{r}(\nu)$ by

$$\hat{r}(\nu) = r(\nu) \exp[-i\theta(\nu)] = r(\nu) \cos \theta(\nu) - ir(\nu) \sin \theta(\nu) = \frac{n(\nu) - 1}{n(\nu) + 1} \quad (83)$$

Let $F_o(x)$ be the background interferogram recorded with the fixed mirror in the specimen arm of the interferometer, and $F_s(x)$ be the interferogram recorded after removing the mirror. Then the complex insertion (reflection) loss $L(\nu)$ becomes

$$L(\nu) = \frac{F\{F_S(x)\}}{F\{F_O(x)\}} = \frac{r_{OS}(\nu)}{r_{OM}(\nu)}, \quad (84)$$

$r_{OM}(\nu)$ and $r_{OS}(\nu)$ are the complex amplitude reflectivity at air-mirror and air-film interfaces respectively and are given by

$$\begin{aligned} r_{OM}(\nu) &= r_{OM}(\nu) \exp[-iph r_{OM}(\nu)] \\ &= r_{OM}(\nu) \exp[-i\theta_{OM}(\nu)] = r_{OM}(\nu) \exp(-i\pi) = -1 \end{aligned} \quad (85)$$

$$\begin{aligned} r_{OS}(\nu) &= r_{OS}(\nu) \exp[-iph r_{OS}(\nu)] \\ &= r_{OS}(\nu) \exp[-i\theta_{OS}(\nu)] = \frac{n(\nu)-1}{n(\nu)+1} \end{aligned} \quad (86)$$

The Fourier transforms of $F_S(x)$ and $F_O(x)$ give complex spectra $s_S(\nu)$ and $s_O(\nu)$

$$s_O(\nu) = F\{F_O(x)\} = s_O(\nu) \exp[-iph s_O(\nu)] \quad (87)$$

$$s_S(\nu) = F\{F_S(x)\} = s_S(\nu) \exp[-iph s_S(\nu)] \quad (88)$$

Eqn (*) can now be written as

$$\begin{aligned} L(\nu) &= L(\nu) \exp[-iph L(\nu)] \\ &= \frac{s_S(\nu)}{s_O(\nu)} = -r_{OS}(\nu) = \frac{n(\nu)-1}{n(\nu)+1}, \end{aligned} \quad (89)$$

The modulus and phase of the insertion loss are then

$$L(\nu) = \frac{s_S(\nu)}{s_O(\nu)} = r_{OS}(\nu), \quad (90)$$

$$phL(\nu) = phs_s(\nu) - phs_o(\nu) = \theta_{os}(\nu) - \pi \quad (91)$$

Eqn. 13 can be rearranged to give

$$\begin{aligned} n(\nu) &= \frac{1 - r_{os}(\nu)}{1 + r_{os}(\nu)} \\ &= \frac{\{1 - r_{os}(\nu)\} \cdot \{1 + r_{os}^*(\nu)\}}{\{1 + r_{os}(\nu)\} \cdot \{1 + r_{os}^*(\nu)\}} \\ &= \frac{1 - \{r_{os}(\nu)\}^2 + 2ir_{os}(\nu)\sin\theta_{os}(\nu)}{1 + 2r_{os}(\nu)\cos\theta_{os}(\nu) + \{r_{os}(\nu)\}^2} \end{aligned} \quad (92)$$

where

$$\theta_{os}(\nu) = \pi - \{phs_s(\nu) - phs_o(\nu)\} \quad (93)$$

$n(\nu)$ and $\alpha(\nu)$ are then calculated from

$$n(\nu) = \frac{1 - \{r_{os}(\nu)\}^2}{1 + 2r_{os}(\nu)\cos\theta_{os}(\nu) + \{r_{os}(\nu)\}^2} \quad (94)$$

$$\alpha(\nu) = -\frac{8\pi\nu r_{os}(\nu)\sin\theta_{os}(\nu)}{1 + 2r_{os}(\nu)\cos\theta_{os}(\nu) + \{r_{os}(\nu)\}^2} \quad (95)$$

By removing the fixed mirror, better complex dielectric permittivity spectra are then acquired.

3.5 Conclusion

The direct measurement of complex dielectric permittivity of materials in sub-millimeter wave and THz frequency range is important because various dielectric materials are now in routine use in lots of applications such as metamaterial, millimeter wave integrated circuitry. Testing in the millimeter wave to terahertz range of the frequency spectrum is extremely difficult. The dispersive Fourier transform technique has been successfully applied to measure the dielectric properties of thin film samples at very high frequency range. With the improved 500 nano-meter step scanning mirror movement in a dispersive Fourier transform spectrometer, the phase shift is highly resolved. In this work, the measurements were carried out on known common thin film samples so that the data obtained can be validated. In the future, various other group of samples can be studied to determine complex dielectric permittivity parameters of those materials. This technique can also be applied for studying more complex thin film samples like ferromagnetic samples. The phase resolution can be improved by further reducing the step size of the scanning mirror. Improvements will be made for the data evaluation so that the reliable value of spectra for the imaginary parts of the permittivity can be presented. In the future the scanning mirror movement step size will be further reduced to 250 nanometers. The smaller step size will allow the direct measurement of the specimen thickness from the recorded interferogram signatures to reduce the uncertainty related to the thickness measurement.

4. Error Analysis

In order to ascertain the applicability of the slotted cavity method and the dispersive Fourier transform technique for the measurement of dielectric thin films, it is essential to take into account any systematic or random errors in the measurement process. Materials with known dielectric properties were studied here. The random error and relative error in the measured permittivity values from the slotted cavity technique are acquired by running the measurements for dozens of times. The random error and relative error are shown in table 13.

Table 13 Random Error in Transverse Slotted Cavity Method

Sample	Random Error	Relative Error
Teflon	0.017	0.8
Mylar	0.023	0.8
Polyphenylene Sulfide	0.025	0.8
Fluoropolymer	0.013	0.7
Polyethylene	0.020	0.9
Black Polyester	0.004	0.1

A comparison between permittivity measured values in this work and other literatures is shown in Table 14. It can be observed that some samples are measured very accurately while others show slight drift from the values of the material real part of permittivity. However the permittivity data are acquired in different frequencies or by

different instruments. This can happen due to a random error arising due to the difference in conditions when the sample was being measured. Since these are very thin samples, it is essential to take extreme care during the measurement procedure. A few sources of error are discussed in this section for each of the measurement technique.

Table 14 Comparison of Permittivity between DFTS, Transverse Slotted Cavity and Other Literature

	Teflon	Mylar
Slotted Cavity	2.096 @ 9 GHz	2.931 @ 9GHz
DFTS(average)	2.062 (300~700 GHz)	2.988 (300~700 GHz)
Previous work	2.09@500GHz [29]	2.98@500GHz [29]
Previous work	2.060±0.004 [30]	3.023 [31]
Previous work	2.057 [32]	3.08 [33]
Previous work	2.09 [34]	3.145 [35]
Previous work	2.06 [36]	3.13 [37]
Previous work	2.07 [38]	
Previous work	2.027 [31]	

Since the thickness of the thin film is used when calculating the permittivity, it is important that the thickness is measured very precisely. Measurements were repeated five times and averaged to determine the exact thickness value. The thickness measurement has an uncertainty of ± 500 nm.

For accurate measurements, it is necessary to ensure that the sample surface is perfectly flat at all times. This was particularly difficult to maintain in the slotted cavity technique. Any bend or curve in the surface of the sample can shift the resonance frequency. The waveguide arrangement was first calibrated to minimize any possible system errors. Thru-Reflect-Line (TRL) method was used to calibrate the network analyzer cables and waveguide connectors. The calibration procedure resulted in return losses as low as -45 dB. For a low-absorbability thin film material, the real permittivity ϵ in transverse slotted cavity technique is determined by $\epsilon = 1 + (L/d)(f_0 - f)/f_0$, where L is the thickness of the slotted waveguide, d is the thickness of the thin film. Frequency measurement in Vector Network Analyzer is accurate to millionth GHz.

High resolution DFTS is an accurate and reliable method capable of reproducing refractive index measurements within 1% of the average values. To obtain better signal to noise ratio, cryogenically-cooled detectors were employed in this study in place of traditional method of using room-temperature detectors. The surface reflection losses can be corrected by iteratively using the computed values of refractive indices. The shift in interferogram positions is calculated using the difference in discrete points of the interferogram with an uncertainty of about 250 nm. The theoretical uncertainty in the calculated real part of dielectric permittivity is about 2%. It can be reduced significantly if an average is taken for many recorded interferogram runs. A distribution of measurement results can then be performed [39].

Random errors were negligible except if an air gap was present within the sample holder. The random errors can be further minimized by repeating the measurements and taking an average value of results. The average error values in absorption coefficient, refractive index, real part of permittivity and imaginary part of permittivity and loss tangent measurements were 25%, 1%, 2%, 30% and 29.9% respectively. The refractive index and real part of permittivity values were found to have significantly less error than the other factors studied. This can be explained. The refractive index and permittivity calculations take in to account both the transmission information as well as signal phase shift. This improves the accuracy of the values obtained.

DFTS is capable of producing the best refractive index and real part of permittivity results. The average value of the refractive index is $(1 + x/2d)$, where x is the shift, and d is the sample thickness. In this measurement, the movement of the active arm in DFTS is improved to 500 nano meter step size. The uncertainty of shift is smaller than 500 nano meter. To measure the thickness of thin film samples, a precision pressure sensitive micrometer is used at 16 positions with uncertainty much smaller than one micrometer. The random error of real part of dielectric permittivity on these thin film materials is smaller than 2% in both techniques where the error mainly comes from the measurement of the thickness. However, DFTS typically produces higher error for absorption coefficient and loss tangent value, because it is a single- or a dual-pass system [40] compared to a many pass resonant structure.

As it can be noticed, the random error found in both measurement techniques on thin films is smaller than 2%. Comparing the real permittivity in this work with other literatures, the real permittivity values of known materials are close to others' work. These two measurement methods can be assumed as precise measurement techniques.

5. Conclusion

Real part of complex permittivity of common thin film samples were accurately determined in microwave and near-millimeter wave (THz) frequencies. The newly developed slotted cavity method and improved DFTS technique are thus established as useful methods to characterize complex permittivity of thin film materials. The slotted cavity method is very convenient for it is easy to insert and the thin film material does not need any external support. The improved 500 nanometer size step gives the dispersive Fourier transform spectroscopy excellent sensitivity and ability to accurately determine the dielectric permittivity over a wide near-millimeter wave (THz) range. The work on thin films composed of known materials validates the ability of precise determination of dielectric permittivity by such techniques. In the future, new samples can be studied using these techniques to determine their material properties and hence suitable applications at this frequency range. An extensive repeated measurements and signal averaging will increase the signal to noise ratio and the Q-factor significantly to allow us the determination of the imaginary part of complex dielectric permittivity and the loss tangent of thin film materials at microwave as well as at terahertz frequencies.

List of Publication

Published:

1. "Dielectric permittivity measurements of thin films at microwave and terahertz frequencies," 2011 41st European Microwave Conference (EuMC)
2. "Dielectric measurements and characterization of impurities of photovoltaic cell materials at millimeter and THz waves," 2011 36th International Conference on Infrared, Millimeter and Terahertz Waves (IRMMW-THz)
3. "Complex permittivity of thin films at millimeter and THz frequencies," 2011 36th International Conference on Infrared, Millimeter and Terahertz Waves (IRMMW-THz)
4. "Precise Fourier Transform Spectroscopy based Measurement of Dielectric Properties of Thin Films at Terahertz Frequency Range," proceedings of 2012 IEEE International Instrumentation and Measurement Technology Conference.
5. "Millimeter Wave Dielectric Spectroscopy and Breast Cancer Imaging," proceedings of 2012 IEEE International Instrumentation and Measurement Technology Conference.
6. "Microwave and Millimeter Wave Ferromagnetic Absorption of Nanoferrites," proceedings of 2012 International Magnetism Conference
7. "Permittivity and Permeability Measurement of Spin-spray Deposited NiZn-Ferrite Thin Film Sample from 18 to 40 GHz," proceedings of 2012 International Magnetism Conference
8. "A Millimeter Wave Breast Cancer Imaging Methodology," 2012 Conference on Precision Electromagnetic Measurements
9. "Precision Measurements of Dielectric Permittivity of Common Thin Film Materials at Microwave and Terahertz Frequencies," 2012 Conference on Precision Electromagnetic Measurements
10. "Microwave and Millimeter Wave Ferromagnetic Absorption of Nanoferrites," IEEE Transaction on Magnetism
11. "Permittivity and Permeability Measurement of Spin-spray Deposited NiZn-Ferrite Thin Film Sample from 18 to 40 GHz," IEEE Transaction on Magnetism

Submitted:

12. "A Millimeter Wave Breast Cancer Imaging Methodology," IEEE Transactions on Instrumentation and Measurement
13. "Precision Measurements of Dielectric Permittivity of Common Thin Film Materials at Microwave and Terahertz Frequencies," IEEE Transactions on Instrumentation and Measurement

Reference

- [1] J. Baker-Jarvis, R. G. Geyer, J. H. Grosvenor Jr, M. D. Janezic, C. A. Jones, B. Riddle, C. M. Weil, and J. Krupka, "Dielectric characterization of low-loss materials a comparison of techniques," *Dielectrics and Electrical Insulation, IEEE Transactions on*, vol. 5, pp. 571-577, 1998.
- [2] B. Chung, "A convenient method for complex permittivity measurement of thin materials at microwave frequencies," *Journal of Physics D: Applied Physics*, vol. 39, p. 1926, 2006.
- [3] H. Jin, S. Dong, and D. Wang, "Measurement of dielectric constant of thin film materials at microwave frequencies," *Journal of Electromagnetic Waves and Applications*, 23, vol. 5, pp. 809-817, 2009.
- [4] A. Vyas, V. Rana, D. Gadani, and A. Prajapati, "Cavity perturbation technique for complex permittivity measurement of dielectric materials at X-band microwave frequency," 2008, pp. 836-838.
- [5] M. N. Afsar, "Dielectric measurements of millimeter-wave materials," *Microwave Theory and Techniques, IEEE Transactions on*, vol. 32, pp. 1598-1609, 1984.
- [6] M. Afsar and H. Chi, "Observation of a doublet ferromagnetic resonance in cubic and hexagonal ferrites at millimeter wavelengths," 1990, pp. 737-738 vol. 2.
- [7] J. Baker-Jarvis, E. J. Vanzura, and W. A. Kissick, "Improved technique for determining complex permittivity with the transmission/reflection method," *Microwave Theory and Techniques, IEEE Transactions on*, vol. 38, pp. 1096-1103, 1990.
- [8] A. Sharma, "Design of Broadband Microwave Absorbers for Application in Wideband Antennas," Master of Science, Electrical and Computer Engineering, TUFTS UNIVERSITY, 2011.
- [9] A. Nicolson and G. Ross, "Measurement of the intrinsic properties of materials by time-domain techniques," *Instrumentation and Measurement, IEEE Transactions on*, vol. 19, pp. 377-382, 1970.
- [10] W. B. Weir, "Automatic measurement of complex dielectric constant and permeability at microwave frequencies," *Proceedings of the IEEE*, vol. 62, pp. 33-36, 1974.
- [11] N. N. Al-Moayed, M. N. Afsar, U. A. Khan, S. McCooey, and M. Obol, "Nano ferrites microwave complex permeability and permittivity measurements by T/R technique in waveguide," *Magnetics, IEEE Transactions on*, vol. 44, pp. 1768-1772, 2008.
- [12] M. N. Afsar, X. Li, and H. Chi, "An automated 60 GHz open resonator system for precision dielectric measurements," *Microwave Theory and Techniques, IEEE Transactions on*, vol. 38, pp. 1845-1853, 1990.

- [13] C. Rubinger and L. Costa, "Building a resonant cavity for the measurement of microwave dielectric permittivity of high loss materials," *Microwave and Optical Technology Letters*, vol. 49, pp. 1687-1690, 2007.
- [14] R. Coccioli, G. Pelosi, and S. Selleri, "Characterization of dielectric materials with the finite-element method," *Microwave Theory and Techniques, IEEE Transactions on*, vol. 47, pp. 1106-1112, 1999.
- [15] Y. Xu and R. G. Bosisio, "Analysis of different coaxial discontinuities for microwave permittivity measurements," *Instrumentation and Measurement, IEEE Transactions on*, vol. 42, pp. 538-543, 1993.
- [16] M. Hussain, "Mathematical model for the electromagnetic conductivity of lossy materials," *Journal of electromagnetic waves and applications*, vol. 19, pp. 271-279, 2005.
- [17] B. Viswanathan, R. Raman, N. Raman, and V. Murthy, "Microwave power loss and XPS measurements on high Tc Nd---Ba---Cu---Oxide superconducting system," *Solid state communications*, vol. 66, pp. 409-411, 1988.
- [18] V. Murthy and R. Raman, "A method for the evaluation of microwave dielectric and magnetic parameters using rectangular cavity perturbation technique," *Solid state communications*, vol. 70, pp. 847-850, 1989.
- [19] B. Meng, J. Booske, and R. Cooper, "Extended Cavity Perturbation Technique to Determine the Complex permittivity of dielectric materials," *Microwave Theory and Techniques, IEEE Transactions on*, vol. 43, pp. 2633-2636, 1995.
- [20] A. Parkash, J. Vaid, and A. Mansingh, "Measurement of dielectric parameters at microwave frequencies by cavity-perturbation technique," *Microwave Theory and Techniques, IEEE Transactions on*, vol. 27, pp. 791-795, 1979.
- [21] R. Waldron, "Perturbation theory of resonant cavities," *Proceedings of the IEE-Part C: Monographs*, vol. 107, pp. 272-274, 1960.
- [22] C. Qian and W. Dou, "A new approach for measuring permittivity of dielectric materials," *Journal of electromagnetic waves and applications*, vol. 19, pp. 795-810, 2005.
- [23] A. Bogle, M. Havrilla, D. Nyquis, L. Kempel, and E. Rothwell, "Electromagnetic material characterization using a partially-filled rectangular waveguide," *Journal of electromagnetic waves and applications*, vol. 19, pp. 1291-1306, 2005.
- [24] J. Roumeliotis, "Resonant frequencies in an electromagnetic rectangular/cylindrical/spherical cavity with an inner off-axis small dielectric sphere," *Journal of electromagnetic waves and applications*, vol. 11, pp. 185-195, 1997.
- [25] J. A. Roumeliotis and G. C. Kokkorakis, "Eigenfrequencies of an electromagnetic rectangular cavity with an inner small sphere," *Journal of the Franklin Institute*, vol. 330, pp. 525-549, 1993.

- [26] J. A. Roumeliotis and G. C. Kokkorakis, "Resonant frequencies in an electromagnetic cylindrical/spherical cavity with an internal off-axis small dielectric sphere," *Electromagnetics*, vol. 14, pp. 195-215, 1994.
- [27] R. F. Harrington, "Time-Harmonic Fields," *New York: McGraw-Hill*, 1961.
- [28] J. Chamberlain, M. N. Afsar, D. K. Murray, G. D. Price, and M. S. Zafar, "Submillimeter-Wave Dielectric Measurements on Absorbing Materials," *Instrumentation and Measurement, IEEE Transactions on*, vol. 23, pp. 483-488, 1974.
- [29] Y. S. Jin, G. Kim, and S. Jeon, "Terahertz dielectric properties of polymers," *Journal of the Korean Physical Society*, vol. 49, pp. 513-517, 2006.
- [30] A. Enders, "An accurate measurement technique for line properties, junction effects, and dielectric and magnetic material parameters," *Microwave Theory and Techniques, IEEE Transactions on*, vol. 37, pp. 598-605, 1989.
- [31] M. N. Afsar, I. I. Tkachov, and K. N. Kocharyan, "A novel W-band spectrometer for dielectric measurements," *Microwave Theory and Techniques, IEEE Transactions on*, vol. 48, pp. 2637-2643, 2000.
- [32] G. L. Friedsam and E. Biebl, "Precision free-space measurements of complex permittivity of polymers in the W-band," 1997, pp. 1351-1354 vol. 3.
- [33] D. C. Dube and R. Natarajan, "Measurement of the permittivity of films at microwave frequencies," *Journal of Physics E: Scientific Instruments*, vol. 7, p. 256, 1974.
- [34] J. W. Lamb, "Miscellaneous data on materials for millimetre and submillimetre optics," *International Journal of Infrared and Millimeter Waves*, vol. 17, pp. 1997-2034, 1996.
- [35] G. E. Conklin, "Measurement of the Dielectric Constant and Loss Tangent of Isotropic Films at Millimeter Wavelengths," *Review of Scientific Instruments*, vol. 36, pp. 1347-1349, 1965.
- [36] F. Shimabukuro, S. Lazar, M. Chernick, and H. Dyson, "A quasi-optical method for measuring the complex permittivity of materials," *Microwave Theory and Techniques, IEEE Transactions on*, vol. 32, pp. 659-665, 1984.
- [37] D. C. Dube and R. Natarajan, "Determination of dielectric parameters for films at microwave frequencies," *Journal of Applied Physics*, vol. 44, pp. 4927-4929, 1973.
- [38] M. Nurul Afsar, "Precision millimeter-wave measurements of complex refractive index, complex dielectric permittivity, and loss tangent of common polymers," *IEEE Transactions on Instrumentation Measurement*, vol. 36, pp. 530-536, 1987.
- [39] C. F. Dietrich, *Uncertainty, calibration, and probability: the statistics of scientific and industrial measurement*: Taylor & Francis, 1991.
- [40] M. N. Afsar, A. Moonshiram, and Y. Wang, "Assessment of random and systematic errors in millimeter-wave dielectric measurement using open resonator and Fourier transform spectroscopy systems," *Instrumentation and Measurement, IEEE Transactions on*, vol. 53, pp. 899-906, 2004.